STUDY OF MAGNETIZED RADIO-FREQUENCY SHEATHS USING KINETIC SIMULATIONS

Ms. Aoife Somers BSc MSc

A dissertation submitted in fulfilment of the
requirements for the award of
Doctor of Philosophy (Ph.D.)

presented to the

School of Physical Sciences
Dublin City University

Supervisors:
Prof. Miles Turner
Dr. Huw Leggate

September 2020

Declaration

I hereby certify that this material, which I now submit for assessment on the programme of study leading to the award of Doctor of Philosophy is entirely my own work, and that I have exercised reasonable care to ensure that the work is original, and does not to the best of my knowledge breach any law of copyright, and has not been taken from the work of others save and to the extent that such work has been cited and acknowledged within the text of my work.

Signed : _____ ID No: 14213070 Date: 11th September 2020

This thesis is dedicated to my grand-parents, Pat and Philomena, for their endless support and encouragement.

Contents

Acknowledgements

The present research work could not have been completed without the support of the following people whom I wish to thank. First and foremost, I would like to thank my supervisor Prof. Miles Turner for the opportunity to undertake this PhD and for his patience and guidance over the years. I also want to thank him for giving me numerous occasions to present my work at conferences. I would also like to thank my secondary supervisor, Huw Leggate, who genuinely helped me find my feet throughout this whole journey. I would like to thank the guys in our group, David, Adam and Rhys. Over the years, David and Adam have helped me to always look on the bright side which is essential at some time or another and Rhys's enthusiam has been refreshing. I would like to think I have provided the group with entertainment with my approach to stressful situations at times. In addition, I would like to thank many of my colleagues (past and present) such as Cleo, Deirdre, Claire, Conor, Ronan, Paul, Brian, Louis, Stephen, and Ben and everyone that frequents the memorial room, which has hosted the most unusual dis-

cussions at times. I would also like to thank all of the academic staff in DCU who have helped me over the years. Thanks to the admisistrative staff Sarah, Sheila, Micheal and school secretary Lisa for all their help over the years. Special thanks to Jonny Hobson for my constant questions - PGR's will forever haunt me. I also need to thank Shikha and Shantanu in IPR, India for their work over the years.

Much commitment, time, effort and sacrifice is required to complete a PhD, and so I owe many thanks to my group of friends for understanding my absense during numerous events. A constant throughout my PhD was my Poppy, my four-legged best friend. Every day she sat while I worked and provided entermainment or comfort when I needed it, as they say the best therapist has four legs and fur. Finally, I would like to thank my family. I am particularly grateful to to my grand-parents, Pat and Phil, for their support throughout not just my PhD but my whole academic career. They predicted this path for me after my first week as an undergraduate and they never lost faith in me and alway encouraged me to do my best. For their support I'll be forever grateful and I dedicate this thesis to them.

List of Figures

LIST OF FIGURES

List of Tables

Abstract

Aoife Somers

Study of magnetized radio-frequency sheaths using kinetic simulations

Plasma sheaths are present wherever a plasma interacts with a surface. In many practical situations, such as in nuclear fusion devices, the sheath is interspersed with an external magnetic field that intersects the surface at some angle. This thesis focuses on the behaviour of magnetized RF sheaths in an RF-CCP discharge since similar RF processes occur near RF antennas in fusion devices. Sheaths represent one of the oldest problems in plasma physics. While there is an abundance of research on sheaths, it is mainly focused on the un-magnetized case or that with a transverse magnetic field. There is less research on the behaviour of sheaths in oblique magnetic fields. RF sheaths are thought to be the cause of numerous, unwanted, deleterious interactions in tokamaks, thereby limiting the performance of RF antennas. Understanding their behaviour is crucial for nuclear fusion research while also having applications in the plasma processing industry where magnetic fields are often employed to enhance reactor performance. The sheath influ-

ences particle and energy fluxes to the surface and can ultimately affect the behaviour of the overall plasma. As a whole, knowledge of sheaths is vital to the understanding of plasma-surface interactions. We used a 1d3v electrostatic particle-in-cell (PIC) code, MagPIC, developed at DCU, to conduct our research. A kinetic study of the sheath is essential in order to capture the small scale kinetic and non-local effects. We have found a magnetized electron series resonance(MESR) can be induced in the presence of an oblique magnetic field. The occurrence of such a resonance is sensitive to the magnetic field angle and occurs only for an extremely narrow range of angles. We have demonstrated that during resonance the ion flux and energy can become decoupled. Upon optimization of parameters, this may provide an alternative method to realise independent control of ion properties, which may lead to applications in plasma processing. We also investigated the applicability of simple sheath models in describing the magnetized situation. From a comparison of our simulation results with a simple RF sheath model that ignores the magnetic field, it was found that such simple models can offer an adequate description of the magnetized situation for an oblique magnetic field. A brief comparison between 1D simulations and experimental results provided by the group in the Institute of Plasma Research (IPR), Gandhinagar, Gujarat, India was also considered. From which we recommend a 2D investigation is needed.

CHAPTER 1

Introduction

1.1 Energy demand and Nuclear fusion

It is estimated that over the next 50 years, the global demand for energy may double in countries such as China and India, which means increasing amounts of power will be needed. Maintaining a reliable and secure energy supply is essential for humankind, and this is where nuclear fusion power can play an essential role and become a significant contributor to the world's energy supply. Nuclear fusion is the process that powers the Sun and the stars. It is the process in which two light nuclei fuse to form a heavier nucleus, which has less mass than the initial two; the missing mass is released as energy. It is this release of energy that makes it appealing as a carbon-free energy source[7]. The Sun burns Hydrogen at around 15 million degrees and confines its plasma with its gravitational field. Trying to re-create similar conditions here on

Earth is difficult. The temperature in a fusion reactor needs to be around 100 million degrees, and its plasma must be confined with strong magnetic fields. The ultimate goal in nuclear fusion research is to have a fusion power plant that will use the energy released during fusion reactions to produce steam and then generate electricity by way of turbines and generators, just like a conventional power plant[8]. The advantages of nuclear fusion power include having a carbon-free energy source, no long-lived radioactive waste, and an almost unlimited supply of fuel on Earth. A huge step in realising this goal is the International Thermonuclear Experimental Reactor (ITER). ITER is a worldwide scientific experiment involving China, the European Union, India, Japan, Korea, Russia, and the United States, all collaborating to build the world's largest nuclear fusion device - a tokamak - in Cadarache, France. A tokamak is a torus-shaped device that uses powerful magnetic fields to confine the plasma in order to reach thermonuclear temperatures. The main goal of ITER is to confirm the feasibility of nuclear fusion as a power source and provide the physics basis for the design of a future nuclear fusion power plant DEMO[9].

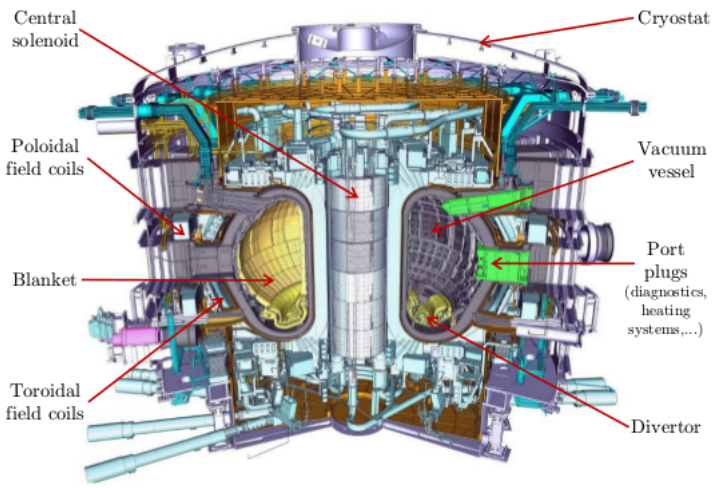

Figure 1.1: Schematic layout of the ITER Tokamak showing inner components of the device[1].

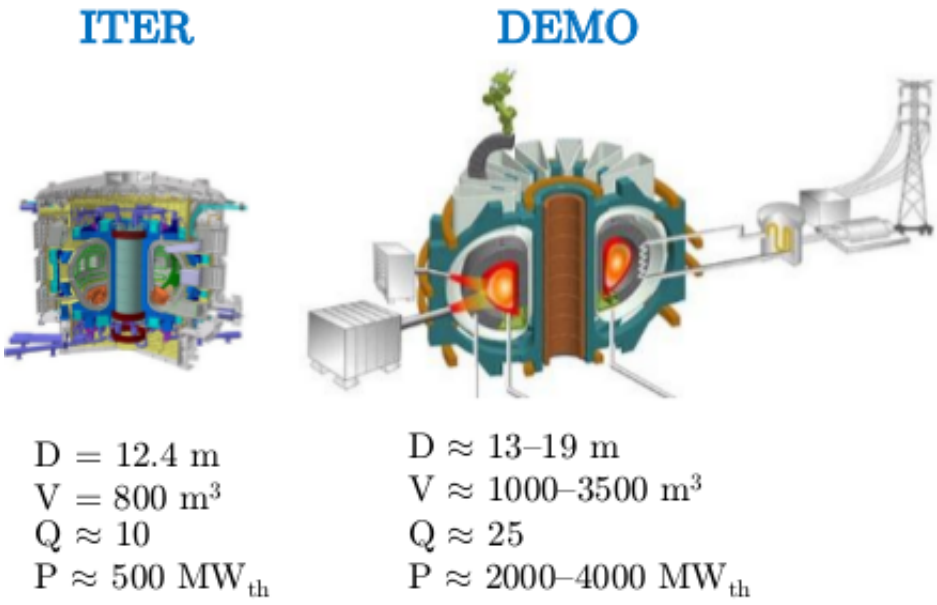

Figure 1.2: Comparison of ITER and DEMO.[1].

1.2 Radio-frequency heating in fusion research

Initial heating of fusion plasmas is provided by Ohmic heating. However, as the plasma temperature rises, the plasma resistivity decreases as $T_e^{-3/2}$ and the role of ohmic heating becomes less important. As a result, additional methods of heating are required to reach thermonuclear conditions. One such method is Ion Cyclotron Resonance Heating (ICRH). It is one of the main auxiliary heating methods used in present-day tokamaks and is also envisaged for both ITER and DEMO[10][11]. The concept of ICRH is based on transferring power from an external antenna to the plasma by launching waves with a frequency that matches the cyclotron frequency, or harmonics, of ions in the plasma, that then allows for collision-less resonant heating of the ions. While ICRH has proven to be effective for plasma heating, the operation of this heating system can lead to the formation of RF sheaths at the antenna. These sheaths are thought to be the cause of numerous, unwanted, deleterious interactions that have been noted on various machines such as erosion, sputtering, hot spot formation, and impurity generation[12][13][14][15]. These effects can reduce the heating efficiency, degrade the quality of the plasma, and can cause damage to the antenna itself thereby setting operational limits for the heating system. These sheaths control the flux and energy of particles to the boundary surface and are interspersed with a magnetic field that intersects the edge components at an oblique angle. Therefore they play an integral role in plasma-surface interactions, not only in fusion devices but in many other practical situations. Hence, the behaviour of magnetized plasma sheaths is the focus of this thesis. The following sections provide an introduction to relevant plasma theory, i.e., various plasma parameters that are commonly used to define characteristics of a plasma.

1.3 Plasma Parameters

The term "plasma" was first coined by Irving Langmuir from his study of ionized gases in 1927. *"We shall use the name plasma to describe this region containing balanced charges of ions and electrons"*[16]. A plasma can be defined as a collection of free, charged and neutral particles, and can be considered the fourth state of matter. Plasma occurs naturally on Earth in the form of lightning as well as the Aurora Borealis. Our Sun and the stars are composed of plasma along with the majority of the visible Universe[17]. Since a plasma consists of charged particles it is strongly influenced by electric and magnetic fields while also being a good conductor. A plasma is an ionized gas, however, not all ionized gases can be classified as plasmas, certain criteria need to be satisfied:

1. The Debye length is small compared to the physical size of the plasma, i.e., $\lambda_D << L$
2. $N_D >> 1$
3. $\omega_c/\omega_p >> 1$

where λ_D is the Debye length (defined in Section 1.3.2) , L is the dimension of plasma, N_D is the number of particles in the Debye sphere, ω_p is the plasma frequency and ω_c is the electron-neutral collision frequency[18]. The application of plasmas can be found in many areas including industry, medicine, space exploration and fusion research [19] [20] [21].

1.3.1 Quasi-neutrality

As a plasma is composed of charged particles it is highly conductive and can be influenced by electromagnetic fields. A definitive property of a plasma is the ability to maintain relatively equal ion and electron densities, $n_e \simeq n_i$, which is known as quasi-neutrality. Due to this property a plasma can be regarded as electrically neutral.

1.3.2 Debye Length

The Debye length, λ_D, is an important property for the description of a plasma. In order to maintain quasi-neutrality, plasmas are capable of shielding an electric field that has been introduced to the plasma. This ability to reduce electric fields is known as Debye shielding, it is also an example of the collective behaviour of plasmas[22]. The distance over which this shielding occurs is called the Debye length, which is essentially the maximum distance over which a plasma can deviate from charge neutrality.

$$\lambda_D = \sqrt{\frac{\epsilon_0 k_B T_e}{n_e e^2}} \tag{1.1}$$

where ϵ_0 is the permittivity of free space, k_B is the Boltzmann constant, T_e is the electron temperature, n_e is the electron density and e is the electric charge.

1.3.3 Plasma frequency

When the electrons in a plasma are perturbed from a uniform background of ions, electric fields begin to build up in an attempt to restore neutrality. This results in the electrons being drawn back to their original positions

but due to their inertia, they overshoot and oscillate about their equilibrium positions[23]. The frequency of this oscillation is known as the plasma frequency, ω_p. Each species has its own frequency but in general when one mentions plasma frequency it refers to the electron plasma frequency, which is the most fundamental time-scale in plasma physics.

$$\omega_p = \sqrt{\frac{n_0 e^2}{\epsilon_0 m_e}} \tag{1.2}$$

where $n_0 = n_e = n_i$ is the plasma density and m_e is the electron mass.

1.3.4 Plasma Potential

The plasma potential, ϕ_p, can be defined as the average potential in the space between charged particles, also called the space potential. In a quasi-neutral plasma the plasma potential is constant since the ion and electron densities are almost equal. However, if an electrode is introduced into the plasma, the ions and electrons interact through repulsions and attractions and its potential will be less than the plasma potential due to the development of a Debye sheath[24].

1.3.5 Collision Frequency

The collision frequency describes the rate of collisions between two particles in a given volume, per unit time. In particular, electron-neutral collisions are the most representative physical phenomena of a plasma system. The average distance a particle travels between successive collisions is known as the mean-free-path, λ_{mfp} [25].

1.3.6 Gyro-frequency

Since a plasma is composed of charged particles it is influenced by electric and magnetic fields. When a magnetic field is present, the magnetic force acts perpendicular to the velocity of the charged particles, causing the particles to rotate around the magnetic field lines. The frequency of this rotation is known as the gyro-frequency, ω and is given by:

$$\omega = \frac{|q|B}{m_s} \tag{1.3}$$

where q is the electric charge, B is the magnetic field strength and m_s is the mass of the species under consideration.

1.3.7 Gyro-radius

The gyro-radius of a charged particle is defined as the radius of circular motion it makes as it gyrates around a magnetic field line. Ions and electrons gyrate in opposite directions around magnetic field lines. The stronger the magnetic field the tighter charged particles are tied to the field lines resulting in a smaller gyro-radius.

$$\rho_s = \frac{m_s v_\perp}{|q|B} \tag{1.4}$$

m_s is the mass of the species, $v_\perp$ is the perpendicular velocity.

1.4 Plasma Sheaths

1.4.1 Sheath formation

A sheath is a charged boundary layer that forms at any plasma-boundary interface. When a plasma comes into contact with an un-biased surface, the electrons being more mobile than the ions, leave the plasma faster and charge the surface negatively with respect to the plasma. This negative potential sets up an electric field that attracts ions and repels electrons, forming a region of positive space-charge in front of the surface, that works to equalize fluxes to that surface. The potential at which the flux of ions and electrons is equal at the surface is known as the floating potential, ϕ_f, which is less than the plasma potential. Quasi-neutrality no longer holds in the sheath and it has a width of several Debye lengths[26].
Sheaths are considered to be one of the most fundamental structures in plasma physics and as a result, have been studied extensively for decades[27] [28] [29]. They are present in any situation where a plasma comes into contact with a surface, for instance, at the edge of nuclear fusion devices, the interface between spacecrafts and space plasma, as well as being widely utilised in the plasma processing industry[30][31].

One cannot discuss sheaths without mentioning the Bohm criterion[32]. In 1949 Bohm introduced a criterion for stable sheath formation. He proposed that the formation of a stable sheath is only possible when ions enter the sheath with a perpendicular velocity greater than the ion sound speed, which is known as the Bohm velocity, v_B, given by:

$$v_B = \sqrt{\frac{eT_e}{m_i}} \tag{1.5}$$

where e is the electric charge, T_e is the electron temperature and m_i is the ion

mass. The Bohm criterion assumes a single species of mono-energetic ions, a Boltzmann distribution for electrons, collisionless ion motion within the sheath and the electric field is zero at the plasma-sheath edge. Ionization is also neglected. Bohm concluded the point at which the ions reach the sound speed, defines the sheath edge location. In order to accelerate the ions to such a speed an additional layer with a small non-zero electric field called the pre-sheath, has to exist in front of the sheath. This pre-sheath layer is still quasi-neutral and much larger compared to the sheath itself. Therefore, a confined plasma can generally be divided into the bulk plasma and sheath region, both with very different characteristics and length scales, and the sheath region further divided into sheath and pre-sheath regions.

In an RF plasma, the frequency of the applied RF voltage ω_{rf}, is in the range between the ion and electron plasma frequency, $\omega_{pi} < \omega_{rf} < \omega_{pe}$. Generally, this is the frequency range used in industrial and laboratory plasmas. In this situation, the electrons can follow the oscillations of the RF electric field while the more massive ions can only respond to the time-averaged field. Due to the RF voltage over the electrodes, the sheath voltage is RF modulated and the sheath thickness will oscillate at the RF frequency[33]. RF plasmas are advantageous, particularly in industry, as they can be operated at much lower pressures, they are more efficient at promoting ionisation and sustaining the discharge compared to DC discharges.

1.4.2 Magnetized Sheaths

As already mentioned, a confined plasma can be divided into the bulk plasma and the sheath region. In the presence of a magnetic field another region, the magnetic pre-sheath appears. The introduction of a magnetic field makes the behaviour of plasma and the sheath more complicated, with the magnetic field angle and magnitude influencing the sheath structure[34]. A plasma is classified as being magnetized when the magnetic field is strong enough to influence the particles trajectories and the gyro-radius of the particles is considerably smaller than the overall size of the plasma $\rho << L$. Generally, the lighter electrons are more easily magnetized than the more massive ions[35].

Chodura[36] was the first study the behaviour of sheaths with an oblique magnetic field. As a result, he postulated the existence of an additional layer, called the magnetic pre-sheath or Chodura sheath, that forms ahead of the Debye sheath, in order to satisfy sheath formation in the presence of oblique magnetic field. In this region quasi-neutrality still holds and it scales with the ion gyro-radius, ρ_i. The function of the magnetic pre-sheath is to turn the direction of the ions from traveling in the direction parallel to the magnetic field when entering the magnetic pre-sheath, to the direction perpendicular to the surface upon leaving the magnetic pre-sheath. This is achieved by the strong electric field in the magnetic pre-sheath. Chodura introduced his own criterion which is essentially the Bohm criterion with an oblique magnetic field known as the Bohm-Chodura criterion. This requires that the ion velocity parallel to the magnetic field must reach the ion sound speed at the entrance to the magnetic pre-sheath:

$$v = c_s \cos\psi \tag{1.6}$$

where c_s is the ion sound speed, $c_s = \sqrt{\frac{k_B(T_e+T_i)}{m_i}}$, and ψ is the angle the

magnetic field makes relative to the electric field. Chodura also determined that the size of the magnetic presheath is dependent on the angle of incidence as well as the ion gyro-radius, while the overall potential drop between the wall and plasma is independent of the magnetic field.

Therefore, the magnetized plasma-surface transition region consists of the essentially three regions : (i) the magnetic pre-sheath, (ii) the Debye sheath, and (iii) the pre-sheath as can be seen in Figure 3. The study of sheaths in the presence of an oblique magnetic field is an important area of research due to its relevance. For instance, in nuclear fusion devices such sheaths determine the energy and flux onto the surfaces in contact with the plasma. While in plasma processing, magnetic fields are often used to enhance the reactors performance thereby exploiting the sheath behaviour. Hence, this thesis is dedicated to establishing a better understanding of the behaviour of magnetized sheaths using kinetic simulations, namely a particle-in-cell code, that is described in Chapter 2.

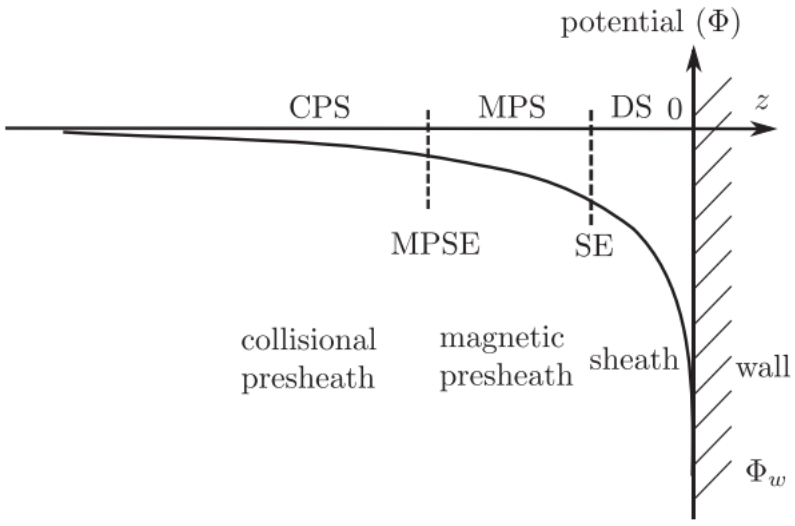

Figure 1.3: Structure of magnetized plasma-wall transition layer[2].

1.5 Thesis outline

The thesis is organised as follows:

- **Chapter 2** provides a general introduction to plasma simulations. Briefly discuss the different branches of plasma simulations and why kinetic simulations are suited for our work. The general algorithm of particle-in-cell simulations is introduced. We provide a description of our 1d3v electrostatic PIC code, MagPIC, developed at DCU.

- **Chapter 3** presents a general overview of RF-CCP discharges. Discuss the limitation of conventional, single frequency CCPs and novel approaches to overcome these limitations. Present our model of a magnetized capacitive discharge along with background theory.

- **Chapter 4** presents our simulation results regarding the plasma series resonance phenomenon.

- **Chapter 5** presents our investigation into the applicability of unmagnetized RF sheath models in describing the magnetized scenario. Introduce the background theory and discuss simulation results.

- **Chapter 6** presents experimental results from an RF-CCP reactor conducted by IPR, India. Experimental setup is briefly explained. Comparisons are made with our 1D MagPIC and experimental results. 2D MagPIC simulation results are also compared with experimental results.

- **Chapter 7** presents the conclusions and an overall discussion of the work to date. Recall the thesis objectives with its motivations. Suggestions for future work.

CHAPTER 2

Particle-in-Cell Simulation

2.1 Plasma Modeling

Plasma simulations began in the early 1960s and have grown in complexity ever since. With the numerous plasma applications, numerical simulations have become an indispensable tool in helping to improve the performances of plasma sources and determining optimum operating conditions, especially in cases where direct measurements are costly or too difficult to carry out[37]. Modeling a plasma is not a simple task. It is not possible to incorporate all aspects of a plasma into one detailed model. Different simulation techniques may be needed for different plasma systems in order to capture the main physics of interest. As a result, simplifying assumptions are widely employed when modeling plasmas[38].

2.1 Plasma Modeling

Plasma simulations can be broadly classified into three categories : (*i*) kinetic, (*ii*) fluid and (*iii*) hybrid simulations. The kinetic description considers individual particle interactions via electromagnetic fields. Particle-in-cell(PIC) simulations are one such type that employs the kinetic description [39][40]. In the PIC method, the plasma is modeled using computer-particles that represent a certain number of real particles, commonly on the order of 10^8 actual particles but there is no generally accepted rule of thumb determining this parameter as of yet[41]. Particle transport is calculated by solving the equations of motion, and collisions are handled using Monte Carlo(MC) methods. This method employs very few simplifying assumptions which lead to detailed models of fundamental processes since they are based directly on particle kinetics as opposed to energy distributions as is employed in the fluid description. A major drawback of this method is the long computation time. This method will be discussed in more detail in Section 2.2.

Fluid simulations reduce the complexities of kinetic description by describing the macroscopic behaviour of plasma through macroscopic quantities such as density, velocity, and mean energy. Fluid models solve the Magnetohydrodynamics (MHD) equations, which are obtained by taking velocity moments of the Boltzmann equation. Fluid simulations are well suited for large scale-problems and are known for their fast computational speed, two and three-dimensional simulations can be run in a reasonable amount of time. However, the major approximation of fluid models involves an assumption regarding the velocity distribution. This can limit their application since such an assumption can result in the failure of capturing some physics[38]. For example, fluid models are adequate for providing the general features of the plasma-wall interface, but they are not capable of capturing non-local particle kinetics. For example, fluid models that neglect sheath effects may employ

less restrictive spatial and temporal resolutions to model physical phenomena of interest, but at the same time such models cannot determine to what extent the plasma-surface interactions alter the macroscopic physics[42].

Hybrid simulations involve a combination of both the kinetic and fluid methods. The speed of fluid simulations combined with the accuracy of the PIC simulations results in a hybrid code that runs faster than PIC codes but slower than fluid codes, with the ability to describe some kinetics more accurately than fluid codes alone. Hybrid simulations consider some of the plasma as a fluid and some as particles. Typically electrons are treated kinetically, while neutrals and ions are treated as a fluid[38][43]. The design of hybrid models typically depends on the particular physics needed to be modelled.

Global models are also often employed within plasma simulations. In a basic global plasma model, the plasma is assumed to be homogeneous, i.e. particle densities and temperatures are equal. Global models can be considered a subset of fluid models since they are based on fluid equations, namely particle balance equations and power balance equations. and provide a macroscopic descriptions of the plasma. In a basic global model, the plasma is assumed to be homogeneous therefore all spatial derivatives are zero. The assumption of homogeneity enhances the computational efficiency of these models. At the same time, this is also their disadvantage and can therefore limit their application. Global models do not capture important information concerning spatial variations and as a result, can lead to quantitative errors[44][45].

To conclude, while there are various simulation techniques available to model plasma behaviour, in order to obtain the most detailed description of the sheath, a kinetic description is needed. Hence, this is why PIC sim-

ulations are particularly well suited to examining sheath behaviour. The remainder of this chapter is dedicated to describing the basic algorithm of a PIC code followed by a description of our 1d3v electrostatic code, MagPIC.

2.2 Introduction to PIC Algorithms

PIC simulations are widely employed in plasma modelling[46][47][48]. Being kinetic in nature, no assumptions are made regarding the particles distribution functions, which is why the PIC method is well suited for investigating the sheath region in particular, where ions and electrons are far from equilibrium. In the PIC method, the plasma is modelled by using a set of computer-particles known as super-particles or macro-particles, that represent a fixed number of real particles. They follow the same trajectory as the species they represent since they have the same charge to mass ratio as the real particles. From some set of initial conditions, the electric and magnetic fields are calculated using Maxwells equations, and then the particles are moved a small distance. PIC codes that solve the full set of Maxwell's equations are known as electromagnetic PIC codes while electrostatic PIC codes only consider Poisson's equation, i.e, only electric fields are considered, magnetic component is neglected. Super-particles move with a finite time step, Δt, and the fields are calculated at the boundaries of a set of finite-sized cells of width, Δx, for each time step. For stability reasons, Δt must be small enough to resolve the smallest time scales in the system which is usually the inverse plasma frequency and the cell size, Δx, also needs to resolve the smallest length scale in the system which is the debye length, λ_D, in order to avoid numerical instabilities, and avoid artificial heating of plasma. Numerical heating is a process whereby the particles in the simulation are accelerated more than they should be, simply due to the finite nature of the PIC method. This artificial heating can be caused by poor choice of time-step, grid-size, or even the number of particles in each cell[49]. Having a cell size larger than the Debye length means that effects will not be seen in the calculated fields. In other words, the finest scales must be resolved everywhere. PIC

codes that are required to satisfy these constraints are known as explicit PIC codes. The PIC method alone does not take particle collisions into account, but they can be included by applying a Monte-Carlo collision(MCC) scheme. A typical cycle for an explicit electrostatic PIC code consists of the following steps:

1. Accumulate the charge and current densities on the grid from particle positions and velocities.

2. Solve Poissons equation on the grid to find the electric potential and the electric field.

3. Interpolate the electric field on the grid to the particles position and from equations of motion to determine new particle positions and velocities.

4. Check for collisions.

5. Repeat this cycle as many time steps as necessary for convergence.

As mentioned earlier, PIC simulations are computationally intensive and are susceptible to errors from discrete particle noise. By attempting to speed up simulations by reducing the number of super-particles, simulating too few particles can introduce noise, which can lead to numerical heating, that will affect the simulation results. A more detailed description of the PIC method can be found in [50].

2.3 Description of MagPIC

2.3.1 Overview

MagPIC is a 1d3v electrostatic PIC code, it resolves one spatial but three velocity components, and includes the effect of an external magnetic field. It simulates a 1D plasma-sheath system in a symmetric parallel plate capacitive discharge with one plate grounded while the other is powered. At the plates absorbing wall boundary conditions for the particles are applied, and secondary electron emission is ignored. The background neutral gas is distributed uniformly at a temperature of 300 K. Particles are loaded at random positions, and initial velocities of all particles are assumed to have a Maxwellian distribution. The magnetic field is of constant strength but the angle, θ, is variable relative to the electric field. The simulation setup is shown in Figure 2.1. Simulations can be operated either current or voltage driven modes. For this work, we have chosen the voltage driven mode. Starting with some arbitrary initial conditions, the system evolves to a steady-state, and the output data is averaged over the radio-frequency. Then the simulations resolve the radio-frequency period with the output data representing one such period during which diagnostics of plasma parameters are performed.

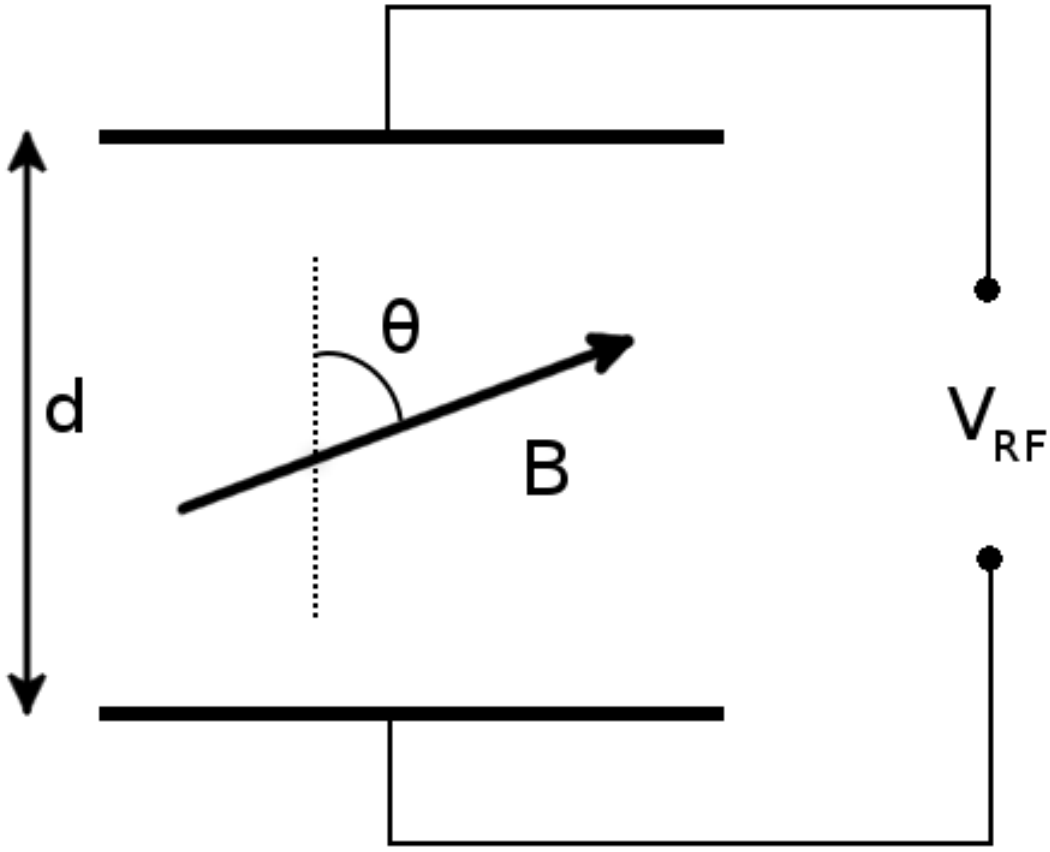

Figure 2.1: Schematic of magnetic field orientation employed by MagPIC, where d is the plate separation and θ is the angle between the magnetic field and the electric field.

2.3.2 Equations of Motion and Particle Pusher

The particle-pusher is the part of the code where the positions and velocities of the particles are updated by integrating the equations of motion[39].

$$m\frac{d\mathbf{v}}{dt} = q(\mathbf{E} + \mathbf{v} \times \mathbf{B}) \tag{2.1}$$

There are several schemes for performing this integration, the most widely used scheme for advancing particles that considers both electric and magnetic fields is the Boris scheme, that is also employed by MagPIC. It is commonly used due to its speed and stability. It is second-order accurate, requires only one field evaluation per time step, and has good conservation properties. It is a leap-frog scheme meaning that particle positions and velocities are staggered by half a time-step, $\Delta t/2$, and the electric and magnetic forces are completely uncoupled. As a result, the equations become time-centered so that they are sufficiently accurate and require relatively short calculation time. The leap-frog scheme is an example of explicit solver, i.e. whereby it depends on old forces from the previous time step. Whereas implicit solvers use the already updated fields, meaning calculation needs more effort and so can be much harder to implement. Boris pusher essentially consists of three separate pushes : (i) a half push by the electric push, Eq. 2.2 then (ii) a rotation by the magnetic field, Eq. 2.4 and then (iii) the second half of electric push, Eq. 2.3.

$$\mathbf{v}^{t-1/2} = \mathbf{v}^{-} - \frac{q\mathbf{E}}{m}\frac{\Delta t}{2} \tag{2.2}$$

$$\mathbf{v}^{t+1/2} = \mathbf{v}^{+} + \frac{q\mathbf{E}}{m}\frac{\Delta t}{2} \tag{2.3}$$

$$\frac{\mathbf{v}^{+} - \mathbf{v}^{-}}{\Delta t} = \frac{\mathbf{v}^{+} - \mathbf{v}^{-}}{2} \times \mathbf{B} \tag{2.4}$$

where $\mathbf{v}^{-}$ and $\mathbf{v}^{+}$ are two intermediate states. Therefore Eq. 2.1 becomes:

$$\frac{\mathbf{v}^{t+1/2} - \mathbf{v}^{t-1/2}}{\Delta t} = \frac{q}{m}\left[\mathbf{E} + \frac{\mathbf{v}^{t+1/2} - \mathbf{v}^{t-1/2}}{2} \times \mathbf{B}\right] \tag{2.5}$$

2.3.3 Field Solver

The function of the field solver within a PIC code is to calculate the electric and magnetic fields on the grid by solving Maxwell's equations, using the charge and current density as sources. In general, the choice of field solver depends on the chosen boundary conditions of the plasma, the geometry of the chamber to be modeled as well as the number of dimensions required in a simulation[39]. Since MapPIC is a 1D, electrostatic code, the differential equations to be solved are:

$$E = -\frac{\partial \phi}{\partial x} \tag{2.6}$$

$$\frac{\partial E}{\partial x} = \frac{\rho}{\epsilon_0} \tag{2.7}$$

which are combined to obtain Poissons equation in 1D:

$$\frac{\partial^2 \phi}{\partial x^2} = -\frac{\rho}{\epsilon_0} \tag{2.8}$$

MagPIC employs a direct solver and so solves the following finite difference equations:

$$E_j = -\frac{\phi_{j+1} - \phi_{j-1}}{2\Delta x} \tag{2.9}$$

$$\frac{\phi_{j+1} - 2\phi + \phi_{j-1}}{(\Delta x)^2} = -\frac{\rho_j}{\epsilon_0} \tag{2.10}$$

Here E is the electric field, ϕ is the potential, ρ is the charge density, ϵ_0 is the permittivity of free space, Δx represents the cell size and j represents

the j^{th} cell. Once the field is known, the particles are indivually advanced in time using equations of motion, with the acceleration found by the interpolation from the electric field on the grid. The steps in the PIC cycle can be represented in Fig. 2.2.

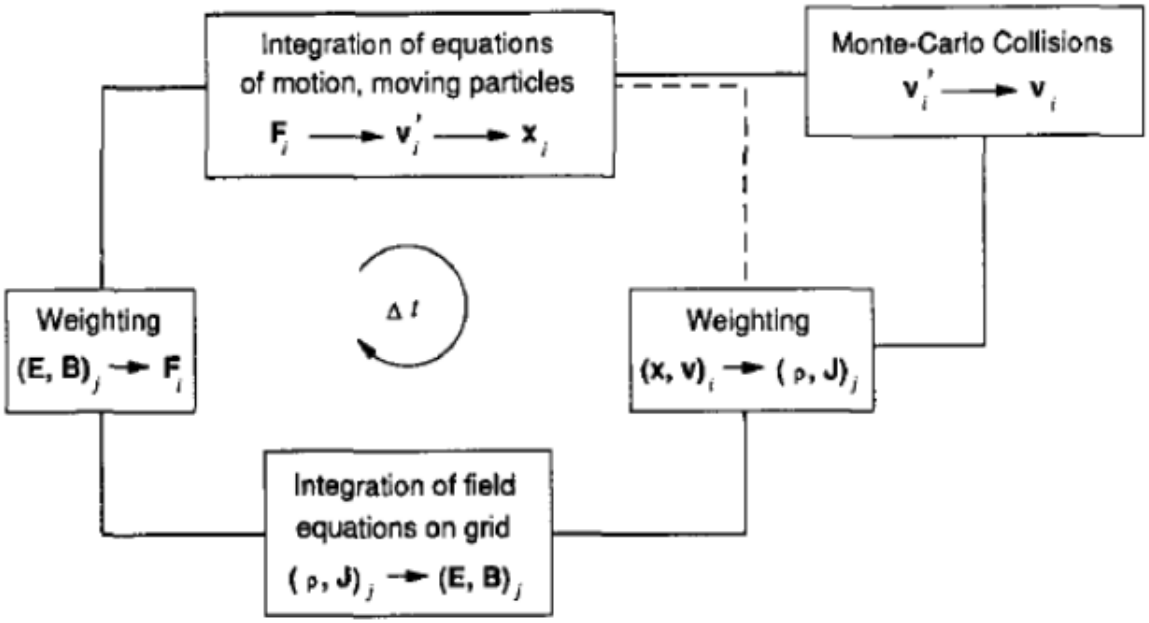

Figure 2.2: Schematic of a typical PIC cycle with Monte-Carlo collisions[3].

2.3.4 Weighting

The PIC method requires a weighting procedure for mapping grid quantities to particle positions and vice versa. The part of the code responsible for this is the weighting scheme that involves interpolation. There are numerous weighting schemes available with different degrees of accuracy and complexity. Zeroth-order weighting is the most basic and assigns a particle's charge to the nearest grid point and imposes the nearest points electric field on that particle. This is also known as nearest-grid-point weighting and is relatively simple and fast meaning it can be noisy. First-order weighting imposes a linear weighting to and from a particle, using the two nearest grid points. In this situation, each particle can be imagined as a cloud of particles that can pass freely through one another. Hence, this scheme is sometimes called the cloud-in-cell scheme. The fraction of the cloud which falls within each grid points sphere of influence is weighted to that cell. As a cloud moves through the gird, it contributes to density much more smoothly, so in comparison to zeroth-order schemes, it smooths the density and potential fluctuations thereby reducing noise[39]. This is the scheme employed by MagPIC for relating grid quantities to particle positions and vice versa. Higher-order weighting schemes are also available but at the cost of more computation.

2.3.5 Collisions

The PIC method alone does not take particle collisions into account, so it must be coupled with a collisional algorithm to account for momentum transfer and charge exchange collisions. This is done by applying a Monte-Carlo collision(MCC) scheme, as is the case in MagPIC. The code handles binary collisions between two particle species, using basically the Direct Simulation Monte Carlo(DSMC) procedure. A random pair of particles are picked and the usual Monte Carlo procedure is applied to determine whether (i) a real collision occurs, and if so, (ii) of what kind. It is assumed that collisions between these species occur with a constant rate k, which is independent of the relative speed of a pair of particles. When dealing with such a large number of particles, computing the probability of a collision occurring for each particle at every time step is computationally demanding, as well as expensive. To overcome this, a fictitious collision known as the null-collision, which is simply just a computational aid, is used. This method provides a constant collision frequency, k, for each particle species, giving a constant collision probability, ν_s, per time step for each species given by Eq. 2.11:

$$P_s = 1 - exp(-\nu_s \Delta t) \approx \nu_s \Delta t \tag{2.11}$$

This means that particles undergoing collisions can be selected at random without the need to compute the collision probability for each particle at every time step. MagPIC considers all important particle interactions like electron-neutral (elastic, inelastic and ionisation) and ion-neutral (elastic, inelastic and charge exchange) collisions using the cross-section data base known as Biagi[51]. Higher order processes like multi-step ionization, particle de-excitation and super elastic collisions are neglected. Therefore, the

procedure within MagPIC consists of picking a random pair of particles and testing for a collision, with a particle only allowed to collide once per time step. Once a collision has occurred, it then has to be determined what type of collision occurs using a random number generator. Those pairs that collided then have their velocites modified in a way that conserves energy and momentum and if necessary, any new particles are added to the simulation.

2.3.6 Sheath widths

The defining of the sheath edge position has been a topic of debate in recent years [52][53] and, an agreed-on definition has yet to be settled on within the plasma physics community. While the most widely accepted definition allows the Bohm criterion to identify the sheath edge alternative definitions have arisen over the years along with complete rejection of the Bohm criterion[54][55][56][57]. Therefore, the conversation around the sheath edge has been shrouded in controversy and, as pointed out by Franklin[29], if this matter is not resolved it is likely to lead to much confusion within the community. In a sense, one can almost compare locating the sheath edge to the location of the edge of a cloud - there is no clear definition. As a result, in this work the sheath edge is defined using three different definitions as follows:

1. The point where the positive space charge in the sheath, n_+, exactly compensates the negative surface charge, $-\sigma$, and the electric field is zero:

$$\int_{electrode}^{sheathedge} n_+(x)dx = -\sigma \tag{2.12}$$

2. The point at which ions reach the Bohm velocity:

$$u_B = \sqrt{\frac{kT_e}{m_i}} \tag{2.13}$$

3. Using the sheath edge ion density, n_s, implied by the ion current, J_i, to determine the sheath edge:

$$J_i = e n_s u_B \tag{2.14}$$

2.4 Summary

In this chapter we gave a brief introduction to plasma simulations and the various models that can be used to model a plasma. Since kinetic simulations are suited for our work, we provide a general description of the particle-in-cell method while also introducing our 1d3v electrostatic PIC code, MagPIC, developed at DCU.

CHAPTER 3

RF-CCP Discharges

3.1 Introduction

A typical RF-CCP discharge consists of two parallel electrodes, placed in a vacuum vessel, powered with a voltage from an RF power source. The RF voltage applied across the electrodes generates an oscillating electric field that accelerates electrons leading to ionization of the working gas resulting in the formation of a plasma. In an RF plasma, the frequency of the electric field is so high that only the electrons can follow the electric field, while the more massive ions remain almost at rest. Sheaths form at the electrodes, and their potential drop and thickness oscillate at the RF frequency. The typical distance between the electrodes is usually between 1-10 cm, while the driving voltage can be between 100 -1000 V. The driving frequency can be between 1 and 100 MHz, but traditionally the conventional frequency of 13.56

MHz is used, which falls in the range between the ion and electron plasma frequencies, $\omega_{ion} << \omega_{RF} << \omega_{pe}$. The pressure of the working gas can vary in the range of 1-1000 Pa, depending on the application of the discharge. RF-CCP discharges can be classified as symmetric or asymmetric. In the case of symmetric discharges, the electrode areas are equal and, this results in the RF voltage being dropped equally across both sheaths. While for asymmetric discharges, the electrode areas are different. Generally, the powered electrode is smaller, and therefore the voltage dropped across the powered sheath is much higher than the voltage across the grounded sheath. i.e., there is an asymmetric voltage distribution[45][33]. Both types of discharge are depicted in Figure 3.1. In principle, CCP discharges operate like a capacitor. The driven electrode corresponds to one of the capacitor plates; the grounded wall of the chamber corresponds to the other plate and, the ionized gas acts like the dielectric.

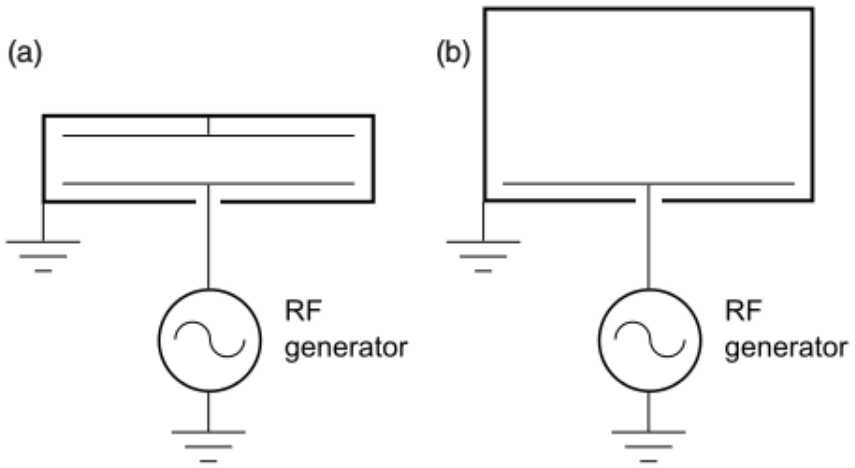

Figure 3.1: Diagram showing a typical (a) symmetric and (b) asymmetric CCP discharge[4].

3.2 Ion Energy and Flux Control

RF-CCP discharges are widely used for plasma-assisted material processing such as plasma etching, deposition, and surface treatment[45]. In these processes, the interaction of energetic ions with the surface play a crucial role. The ion flux is one of the principal parameters in determining the rate of a process at the surface while the ion energy required is largely process dependent therefore independent control of these parameters is desired in plasma processing applications[58]. Consequently, this would allow one to optimize the performance of the discharge. However, conventional, single-frequency CCPs lack this capability since the applied voltage controls both parameters, i.e., increasing the voltage increases both the ion energy and flux simultaneously. Some novel approaches have been adopted in an attempt to overcome this limitation, which will be discussed in the following sections.

Another important parameter is the ion energy distribution function (IEDF) since it provides information about the energy of the ions impinging on the electrodes. The IEDF is mainly controlled by the sheath dynamics, and so plays a crucial role in plasma processing due to its strong influence on the surface reactions. For example, etch profiles are determined by the IEDF, so the ability to control the IEDF is also highly desirable. In this work, dealing with low pressures, we consider the sheaths to be collisionless, $\lambda_{mfp} > s_{width}$, whereas collisional dominated sheaths are a characteristic of discharges with higher pressures i.e., $>$ 10 Pa. For single frequency, CCPs in the collisionless regime, the shape of the IEDF is determined by the ratio of the ion transit time across the sheath, τ_i, to the RF period,τ_{rf}. For $\frac{\tau_i}{\tau_{rf}} << 1$, ions cross the sheath within a fraction of the RF cycle. As a result, they respond to the instantaneous sheath voltage, and so their energy strongly depends on what phase of the cycle they enter the sheath. In

this case, the sheath tends to be resistive, and this is known as the low-frequency regime. In this situation, the IEDF is broad and bimodal, where the two peaks correspond to the maximum and minimum sheath voltage. For $\frac{\tau_i}{\tau_{rf}} >> 1$, ions take many RF cycles to cross the sheath and so respond to the time-average sheath voltage, and the phase of the cycle where they enter the sheath is no longer important. This is called the high-frequency regime, and the sheath tends to be capacitive. In this case, the IEDF is characterized by a single peak determined by the time-averaged sheath voltage[59]. Having highlighted the importance of independent control over ion properties, we now discuss some methods to achieve such control before introducing our proposed method.

3.2.1 Dual Frequency Discharges

One of the first approaches to over-come the limitation of single-frequency CCP discharges involved the use of dual-frequency discharges[60][61][62], where a very high-frequency, e.g. 100 MHz, and a very low-frequency, e.g. 1 MHz, are applied to the discharge. The high-frequency component controls the plasma density and thereby, the ion flux, while the lower frequency component controls the sheath voltage and, ultimately, the ion energy[63]. However, while this approach provides improved control, it has been shown that there can be coupling between the two frequencies if they are too close to each other, and for very high frequencies, electromagnetic effects can arise. Parasitic effects due to secondary electrons can also be introduced, and so the desired separate control of the ion energy and flux is limited to a very narrow parameter range[64].

3.2.2 Electrical Asymmetry Effect

Another approach considers the electrical asymmetry effect (EAE)[65][48][5], whereby the discharge is made electrically asymmetric. In geometrically asymmetric discharges, a DC self-bias automatically develops due to the difference in electrode sizes in order to balance the electron and ion flux to each electrode over one RF period. Whereas in symmetric discharges, no such DC self-bias develops since the voltage distribution is symmetric. The EAE can be employed in a geometric CCP by applying a combination of the fundamental frequency and its second harmonic, thereby inducing an asymmetry which leads to the generation of a DC self-bias. The phase angle, θ, between the two frequencies, is the control parameter and, when adjusted, will adjust the DC self-bias and hence, the energy of the ions, resulting in

control over the ion energy while the ion flux remains constant. An advantage of using this method with geometric discharges means smaller chambers can be used since, in most asymmetric discharges, the chamber is generally much larger than the substrate since it acts as the ground electrode, therefore reducing cost[4]. However, it has been observed that the performance of the EAE is reduced at lower driving frequencies due to enhanced charged dynamics[66].

3.2.3 Voltage Waveform Tailoring

Expanding on the EAE leads to the method of voltage waveform tailoring (VWT), which provides significantly better separate control of the ion energy and flux[67][68][69]. In this situation, the driving voltage waveforms are generated as a superposition of multiple consecutive harmonics of a fundamental driving frequency. The form of these tailored voltage waveforms is chosen to maximize the EAE. As a result, the symmetry of the plasma can be controlled by adjusting the relative phases of the harmonics. In contrast with the EAE, where just two harmonics are considered, it was found as the number of harmonics is increased, the self-bias and ion energy control range also increases. However, at the same time, there is significant waveform distortion as the number of harmonics is increased[70].

3.2.4 Magnetic Asymmetry Effect

Treischmann et al.[71] proposed a relatively new technique, whereby the discharge symmetry is controlled by applying a spatially inhomogeneous magnetic field. When a parallel magnetic field is applied to the electrodes higher at one electrode compared to the other, this will lead to the generation of a DC self-bias, even in geometrically symmetric CCPs. This is due to greater

confinement of electrons in the region of the higher magnetic field leading to enhanced ionization thereby inducing an asymmetry. Electron field reversals during sheath collapse can also occur due to the reduction in the electron mobility to ensure flux compensation of ions and electrons at the electrode. As a result, there is a higher ion density at one electrode compared to the other, which leads to the generation of a DC self-bias. It is this difference in electron confinement at both electrodes that control the symmetry and therefore, the DC self-bias. Hence, by adjusting the magnetic field configuration, one can control the mean ion energies at both electrodes. Simulation studies provided by Yang et al.[72][73] verified the MAE could make a geometrically symmetric CCP asymmetric, although it was found that the effect is reduced at high pressures, while Oberberg et al.[74] provided the first experimental evidence of the viability of MAE.

Each of the methods discussed initially appears to offer independent control over the ion properties, however, they are challenging to implement and are not without their limitations. We offer an alternative method based on a series resonance for a magnetized, single frequency symmetric CCP discharge.

3.3 Plasma Series Resonance

In the following sections, we present a method by which independent control of the ion properties is observed through a series resonance in a magnetized single frequency RF-CCP discharge. We offer a brief introduction into the background theory, followed by a discussion of the magnetized electron series resonance(MESR) phenomenon. We then provide a description of our capacitive discharge model that considers a variable magnetic field angle which is based on coupling a global plasma model with a cold electrical model. Finally, we present our simulation results based on the described model and discuss possible applications and relevance.

3.4 Introduction to Electron Series Resonance

Electron series resonance(ESR), also known as plasma series resonance(PSR) or a plasma-sheath resonance[75], is a phenomenon that was first associated with geometrically asymmetric discharges, represented by Eq. 3.1.

$$\omega_{res} = \omega_{pe}\sqrt{\frac{2\bar{s}}{L}} \tag{3.1}$$

where ω_{pe} is the electron plasma frequency, $2\bar{s}$ is the total time-averaged sheath width, and L is the discharge length. When investigating ESR, it is common practice to use equivalent circuits and impedance characteristics to analyse the plasma, see Figure 3.2. As a result, a CCP discharge can be represented by an equivalent circuit consisting of a capacitor, representing the sheaths, in series with an inductor and resistor, which represent the electron inertia and electron-neutral collisions in the bulk plasma, respectively[76]. The series resonance occurs when the sheath capacitance perfectly balances the plasma inductance and is signified by the imaginary impedance going to zero i.e., the impedance is purely resistive. This effect has been observed computationally[77] as well as experimentally[78][79].

Originally it was thought that the ESR was a feature exclusive to asymmetric CCP discharges solely due to the non-linearity of the sheaths. In the completely symmetric case, the non-linearity of the two sheaths cancels, and so there is no mechanism to produce such resonance. It was then realized by using the methods mentioned earlier to induce an asymmetry that symmetric CCPs could also exhibit such a resonance[80][81][82]. A resonant sustained discharge is advantageous for several reasons; they can be excited by much smaller voltages, thermal loads on the surfaces are reduced, and the input resistance is also low, which means there is maximal power transfer to

the discharge[83][77]. ESR is already known for influencing the ohmic and stochastic heating in RF-CCP discharges at low pressures which can lead to higher densities and etch rates[84][85]. However, in general, ESR is thought to occur at much higher frequencies than the conventional RF driving frequencies, i.e., 13.56 MHz.

In the remainder of this chapter, we demonstrate how a magnetized electron series resonance(MESR) was achieved at this frequency with the application of an oblique magnetic field. It has been previously suggested that this phenomenon may provide a means to control various discharge parameters[**?**]. Therefore, the objective of this section involves investigating the viability of using MESR as a means to achieve independent control over the ion flux and energy. It is this possibility of control over plasma parameters that would make MESR sustained discharges an attractive candidate for plasma processing.

3.5 Magnetized Electron Series Resonance

While ESR discharges have been discussed in the literature[86][82][77], the behaviour of magnetized resonant discharges has received relatively little attention as of yet. Qui[75] provides a detailed study on magnetized resonant discharges supplying both theoretical and simulation work which we will now consider. Ultimately, he derives an equation for the MESR frequency, ω_{mesr} from an equivalent circuit model using cold plasma theory given by:

$$\omega_{mesr}^2 = \frac{\omega_{ce}^2 + \omega_{esr}^2}{2} \pm \sqrt{(\frac{\omega_{ce}^2 + \omega_{esr}^2}{2})^2 - \sin^2\phi\omega_{ce}^2\omega_{esr}^2} \tag{3.2}$$

where ω_{ce}, ω_{esr} and ϕ is the electron cyclotron frequency, electron series resonance frequency and the magnetic field angle with respect to the plate, respectively.

Their work is based on a 1D plasma diode model, whereby the noise current from a decaying uniform plasma is found to exhibit the MESR frequency. Simplifying assumptions such as a static magnetic field, unmagnetized sheaths and neglecting the ion motion are employed. Much the same as ESR, MESR occurs at frequency at which the diode impedance is resistive. Therefore, for resonance to occur the dielectric constant of plasma in a weak magnetic field must be negative, i.e. $\epsilon_r < 0$, to allow for an inductive bulk so as to cancel with the capacitive sheaths. This leads to two frequency branches, a lower branch ω_L (Eq. 3.3) and an upper branch ω_H (Eq. 3.4) and, with a dependence on the magnetic field angle with respect to the plates, ϕ.

$$0 < \omega_L < \omega_{ce}\sin\phi \tag{3.3}$$

$$\omega_{ce} < \omega_H < \sqrt{\omega_{pe}^2 + \omega_{ce}^2 \cos^2 \phi} \tag{3.4}$$

A global model for magnetized resonant discharges is also introduced, allowing one to obtain relations between the discharge parameters. A planar cold homogeneous plasma model is employed[87] where stationary ions uniformly fill the discharge while a cold uniform electron slab neutralizes the ion charge at the center, while electron depleted matrix sheaths form at the plates. The equivalent circuit consists of capacitors representing the electron depleted sheaths, a center capacitor representing the displacement current through the bulk, a resistor representing the electron-neutral collisions and an inductor representing the electron inertia.

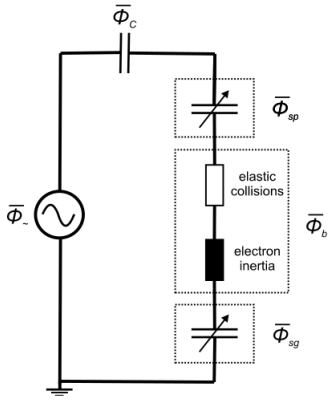

Figure 3.2: Equivalent circuit of RF-CCP discharge taken from [5].

A classic plasma global model is based on two equations: (i) the particle balance equation and (ii) the power balance equation. The electron density is determined by the power balance equation, equating the total power absorbed by electrons (Eq. 3.5) to the total power lost (Eq. 3.6). The electron temperature is determined by the particle balance equation, equating the

total particle loss to the walls to the volume ionisation given by Eq. 3.7. Given n_g and d, the electron temperature can be determined.

$$P^e_{abs} = \frac{I^2_{RF} Z_r}{2} \tag{3.5}$$

where I_{RF} is the RF current and Z_r is the real part of the impedance.

$$P^e_{loss} = 2en_s u_b A(\epsilon_c + 2T_e) \tag{3.6}$$

where n_s is the plasma density at the sheath edge, ϵ_c is the electron collision loss and ionisation loss in the plasma bulk and $2T_e$ is the electron energy loss at the walls.

$$\frac{K_{iz}(T_e)}{u_B(T_e)} = \frac{2\alpha}{n_g d} \tag{3.7}$$

here $K_{iz}(T_e)$ is the electron-neutral ionization rate constant, $u_B(T_e)$ is the bohm velocity, $\alpha = n_s/n_0$, where n_s is the density at the sheath edge and n_0 is bulk plasma density, d is the plasma bulk width and n_g is the neutral gas density.

It is important to remember that while these simple models can provide considerable insight into the behaviour of CCP discharges, thanks to their simplifying assumptions, at the same time they cannot fully predict the quantitative behaviour of real discharges.

3.6 Magnetized Capacitive Discharge Model

In this section, we present a simple model of a magnetized capacitive discharge with variable magnetic field angle, that couples a global plasma balance model with a cold plasma electrical model. We have extended the model of R. Lucken[88] *et al.* allowing for an arbitrary magnetic field angle thereby allowing us to examine a range of angles for which stationary solutions may exist. Luken's model is essentially based around three equations, the electron momentum balance equation (Eq. 3.8), electron continuity equation (Eq. 3.9) and a collisionless momentum conservation equation (Eq. 3.10). From these equations, they derive an equation for the electron temperature (Eq. 3.11) (that can be solved numerically for $\nu_{iz}(T_e)$) and plasma density (Eq. 3.12) for a 1D CCP discharge with a parallel magnetic field.

$$0 = \phi' - \mathbf{v} \times \mathbf{b} - \frac{\mathbf{n}'}{\mathbf{n}} - \nu\mathbf{v} \tag{3.8}$$

$$\frac{\partial n}{\partial t} + \nabla \cdot (n\mathbf{v}) = n\nu_{iz} \tag{3.9}$$

$$\frac{v_x^2}{2\mu} = -\phi \tag{3.10}$$

$$\left[\left(\frac{\alpha\mu}{\nu_{iz}}\right)^{\frac{1}{2}} + \left(\frac{\nu_{iz}}{\alpha\mu}\right)^{\frac{1}{2}}\right] \arctan\left[\left(\frac{\alpha\mu}{\nu_{iz}}\right)^{\frac{1}{2}}\right] - 1 = \frac{\mu^{\frac{1}{2}}\alpha l}{2} \tag{3.11}$$

$$\frac{n}{n_0} = \left(1 + \frac{\alpha {v_x}^2}{\nu_{iz}}\right)^{-\frac{1}{2}\left(1+\frac{\nu_{iz}}{\alpha\mu}\right)} \tag{3.12}$$

where ϕ is the electrostatic potential, $\mathbf{v}$ is the electron fluid velocity, n is the electron density, ν is the electron collision frequency, and $\mathbf{b}$ is the unit vector in the direction of the magnetic field. $\alpha = 1/\nu + \nu$, $\mu = m_e/m_i$, ν_{iz} is the electron impact ionization frequency v_x is the velocity along the x-axis, and l is the plasma length. Lucken[88] *et al.* use normalized units where frequencies are normalized to the electron cyclotron frequency, length dimensions are normalized to the thermal gyro-radius of electrons, velocities are normalized to the electron thermal velocity and the electrostatic potential is normalized to the electron temperature.

Allowing for an arbitrary angle between the magnetic field and and the spatially resolved axis we have:

$$\mathbf{B} = \begin{pmatrix} B_0 \sin\theta \\ B_0 \cos\theta \\ 0 \end{pmatrix} \tag{3.13}$$

Starting with :

$$0 = \frac{q}{m_e}\frac{d\Phi}{dx} - \frac{q}{m_e}\mathbf{v} \times \mathbf{B} - \frac{k_B T_e}{n m_e}\frac{dn}{dx} - \nu\mathbf{v} \tag{3.14}$$

so that we have:

$$0 = \frac{q}{m_e}\frac{d\Phi}{dx} + v_z \omega_c \cos\theta - \frac{k_B T_e}{n m_e}\frac{dn}{dx} - \nu v_x \tag{3.15}$$

$$0 = -v_z \omega_c \sin\theta - \nu v_y \tag{3.16}$$

$$0 = -v_x \omega_c \cos\theta + v_y \omega_c \sin\theta - \nu v_z \tag{3.17}$$

Substituting Eq. 3.16 into Eq. 3.17 and eliminating v_z and re-arranging Eq. 3.15 becomes:

$$0 = \frac{q}{m_e}\frac{d\Phi}{dx} - v_x\left(\frac{\omega_c^2\cos^2\theta}{\omega_c^2\sin^2\theta/\nu + \nu} + \nu\right) - \frac{k_B T_e}{n m_e}\frac{dn}{dx} \tag{3.18}$$

The stationary ion continuity equation is given by:

$$\frac{dv_x}{dx} + \frac{v_x}{n}\frac{dn}{dx} = \nu_i \tag{3.19}$$

The potential is zero when the ion drift velocity is zero so the ion energy conservation equation is:

$$\frac{1}{2}m_i v_x^2 = -q\Phi \Rightarrow v_x\frac{dv_x}{dx} = -\frac{q}{m_i}\frac{d\Phi}{dx} \tag{3.20}$$

Therefore Eq. 3.18 now becomes:

$$0 = -v_x^2\frac{dn_x}{dx} - \alpha\omega_c v_x^2 + \frac{k_B T_e}{m_i}\left(\frac{dv_x}{dx} - \nu_i\right) \tag{3.21}$$

where :

$$\frac{\alpha}{\omega_c} = \frac{m_e}{m_i}\left(\frac{\omega_c^2\cos^2\theta}{\omega_c^2\sin^2\theta/\nu + \nu} + \frac{\nu}{\omega_c}\right) \tag{3.22}$$

Upon further manipulation and the introduction of the following normalizations

$$\omega = \frac{v_x}{u_B}, \qquad s = \frac{x\omega_c}{u_B} \tag{3.23}$$

We end up with an equation of the form:

$$1 - \omega^2 \frac{d\omega}{ds} = \nu/\omega_c + \alpha\omega^2 \tag{3.24}$$

which has a solution of the form:

$$C - s = \frac{\omega}{\alpha} - \frac{(\nu_i/\omega_c + \alpha)\arctan\left(\frac{\sqrt{\alpha}\omega}{\sqrt{\nu_i/\omega_c}}\right)}{\sqrt{\nu_i/\omega_c}\alpha^{\frac{3}{2}}} \tag{3.25}$$

The boundary condition is that $\omega = 0$, at s = 0, C = 0. At the edge of the plasma, at s_m , the Bohm condition is satisfied such that $\omega = 1$ Therefore we have:

$$\left[\left(\frac{\nu_i}{\omega_c\alpha}\right)^{\frac{1}{2}} + \left(\frac{\alpha\omega_c}{\nu_i}\right)^{\frac{1}{2}}\right]\arctan\left[\left(\frac{\alpha\omega_c}{\nu_i}\right)^{\frac{1}{2}}\right] - 1 = \alpha s_m \tag{3.26}$$

which is our version of Eq. 3.11 from Lucken's model, that we use to determine the electron temperature based on the equilibrium condition $K_i(T_e)N = \nu_i$, which a solution to is not always guaranteed. Upon further manipulation of the continuity equation we obtain the following equation for the plasma density:

$$n = n_0\left(1 + \frac{\alpha\omega_c\omega^2}{\nu_i}\right)^{-\frac{1}{2}(1+\frac{\nu_i}{\alpha\omega})} \tag{3.27}$$

The equilibrium solutions are found using brute force searches and iteration schemes, but there is no guarantee that a solution does always exist. The solver scans a range of magnetic field angles and, at each angle, a range of

electron densities looking for stationary solutions. We can then determine a range of parameters such as density, electron temperature, driving current density, ion flux and impedance.

3.7 Conclusions

In this chapter we have emphasized the importance of independent control of the ion energy and flux in relation to plasma processing and discussed some methods to achieve such control. We have introduced a possible method for independent control of ion energy and flux in single frequency CCP discharges, through the application of a magnetic field which induces a resonance effect. Furthermore, we also constructed a model of a capacitive discharge with a variable magnetic field angle.

CHAPTER 4

Simulation Results

4.1 Simulation Parameters

In our simulations the variable control parameters are the driving voltage amplitude V_0, the gas density N, and the magnetic field angle, θ. By first choosing V_0 and N, we then investigate the behaviour of the plasma parameters as we vary the magnetic field angle, θ, and the magnetic field strength B_T. We have considered three different magnetic field strengths - 12, 15 and 20 mT - and varied the magnetic field angle, θ, from 0, i.e. perpendicular to the electrode, up to large angles of θ that correspond to shallow angles with the plates. For all simulations, the discharge was driven with 200 V and the plate separation was kept at a fixed distance of 8 cm while the driving frequency was kept constant at 13.56 MHz. This situation was repeated for three different pressures - 1.035, 2 and 4 Pa. The working gas used was He-

lium and electrons and ions are loaded with a Maxwellian distribution and with initial temperatures of $T_e = 2.59$ eV and $T_i = 0.029$ eV respectively and electrons are considered to be weakly magnetized. A particle is considered magnetized once it satisfies the following two criteria: (i) the particles gyro-radius is much less than the discharge length.

$$\rho_s = \frac{m_s v_\perp}{|q|B}, \quad \rho_s << L \tag{4.1}$$

where m_s is the mass of the particle species , $v_\perp$ is perpendicular velocity, q is the electric charge of the particle species, B is the magnetic field strength and L is the discharge length and (ii) the electron gyro-frequency, Ω_{ce}, is less than the electron plasma frequency, ω_{pe}.

$$\Omega_{ce} = \frac{q_e B}{m_e} \tag{4.2}$$

$$\omega_{pe} = \sqrt{\frac{n{q_e}^2}{\epsilon_0 m_e}} \tag{4.3}$$

$$\Omega_{ce} < \omega_{pe} \tag{4.4}$$

where m_e is the electron mass , n is plasma density and ϵ_0 is the permittivity of free space. Particle weighting and numbers needed to be increased as θ is increased. Large angles of θ correspond to small angles with the plates and such a finite angle can considerably impact the electron mobility. The simulations ran for many thousands of RF cycles in order to reach convergence, by which we mean that parameters no longer vary from cycle to cycle. Simulation parameters are summarised in the Table 4.1. The simulation parameters were chosen in relation to a collaboration with an experiment conducted at IPR, India, which will be discussed in Chapter 5.

Simulation Parameters			
	Case 1	Case 2	Case 3
Driving voltage (V)	200	200	200
Electrode gap (cm)	8	8	8
Driving frequency (MHz)	13.56	13.56	13.56
B-field strength (mT)	12	15	20

Table 4.1: Chosen simulation parameters for this study, investigating 3 different magnetic field strengths for each of the chosen pressures.

4.1.1 Electron density

The simulations show that the plasma density, n_e, is strong function of the magnetic field orientation, with a general tendency towards increasing density as the magnetic field angle, θ, tends towards towards 90 degrees, or in other words, as the angle with the plates, α, tends towards 0. However, this trend is interrupted as the θ approaches roughly 85 degrees, which corresponds to grazing incidence with the plates, and no stationary solutions can be found. Therefore there appears to exist a cut-off angle beyond which the plasma density sharply decreases and stationary solutions can not be found, see Figures 4.1 - 4.3. The increase in density is due to the penetration of the electric field into the bulk. As a result of increased electron collisions, the electron impact ionization in bulk maintains a high plasma density. This is a characteristic of the magnetized electron series resonance[89]. It appears that in the presence of a magnetic field at a certain angle, the resonance is directly excited at the driving frequency.

Resonance is marked by the imaginary impedance crossing zero, i.e., becoming positive, which we observed, see Figures 4.4 - 4.6. Strictly speaking in this work, we are dealing with a quasi-resonant discharge since current and voltage are not exactly in phase. As pressure is increased, the resonance effect is reduced due to the increased number of collisions[90]. We can also see that increasing the magnetic field strength also increases the angle where resonance occurs. It is well known that the application of a magnetic field affects the plasma transport to the walls and is accompanied by a drop in the electron temperature and rate of ionization[91], both of which were observed in our simulations. Only at the highest pressure is a plasma sustained for all angles and without a magnetic field since, at higher pressure, the plasma is more confined. Below 4 Pa, a plasma cannot be sustained without a mag-

netic field or below an angle of 53 degrees since the ionization rate is not sufficient to sustain the discharge.

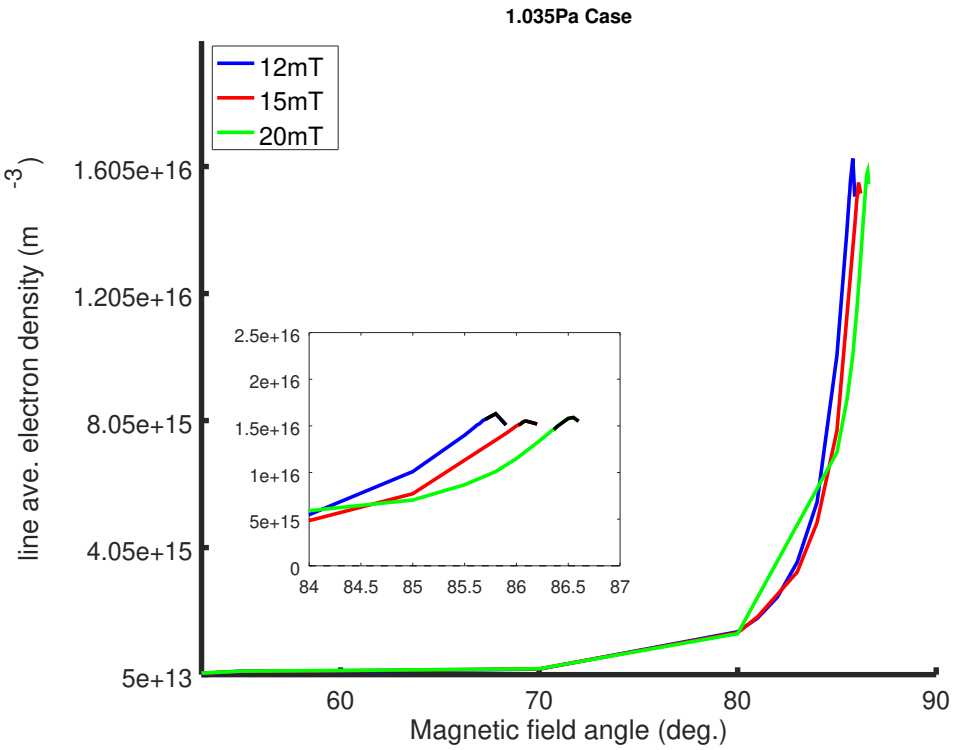

Figure 4.1: Variation of electron density with magnetic field angle, for 1.035 Pa case, where black segments signifiy resonance.

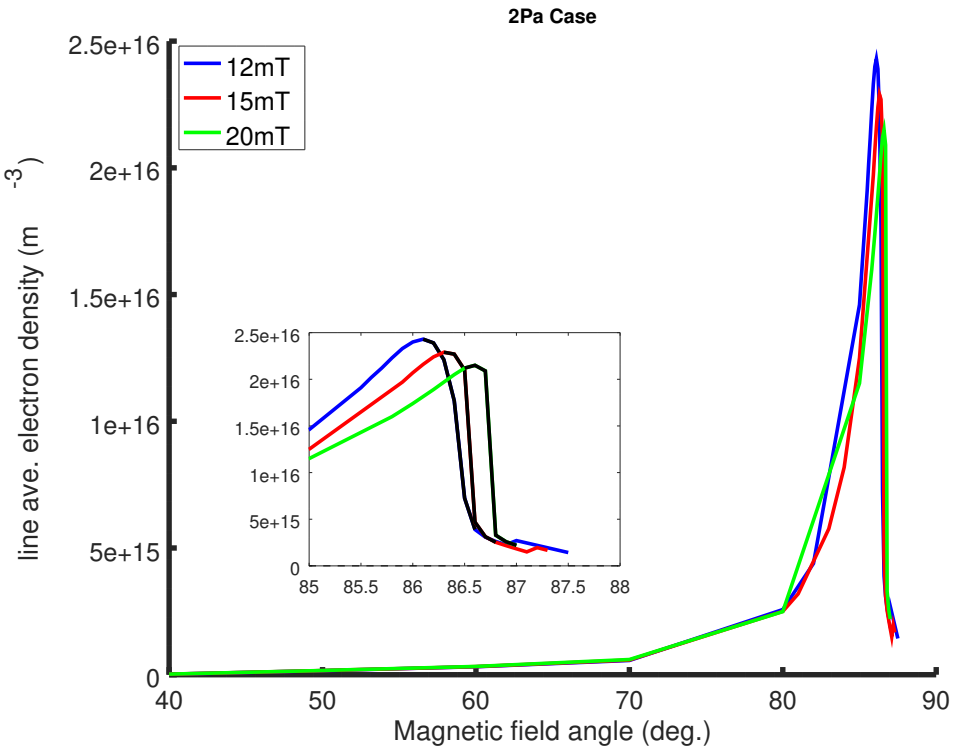

Figure 4.2: Variation of electron density with magnetic field angle, for 2 Pa case, where black segments signifiy resonance.

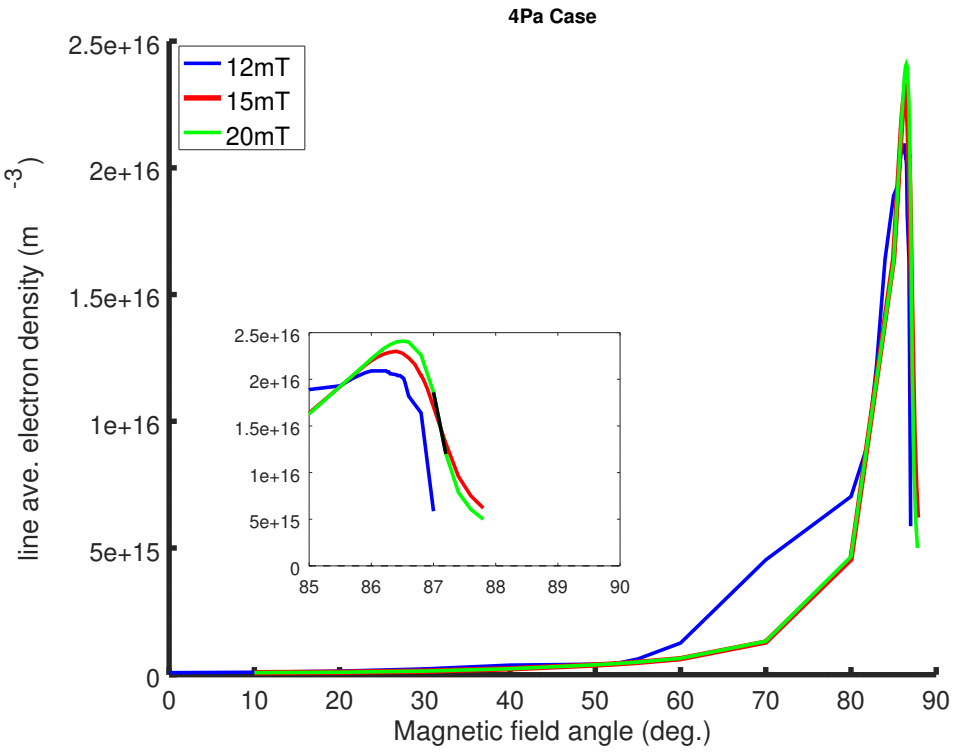

Figure 4.3: Variation of electron density with magnetic field angle, for 4 Pa case, where black segments signifiy resonance.

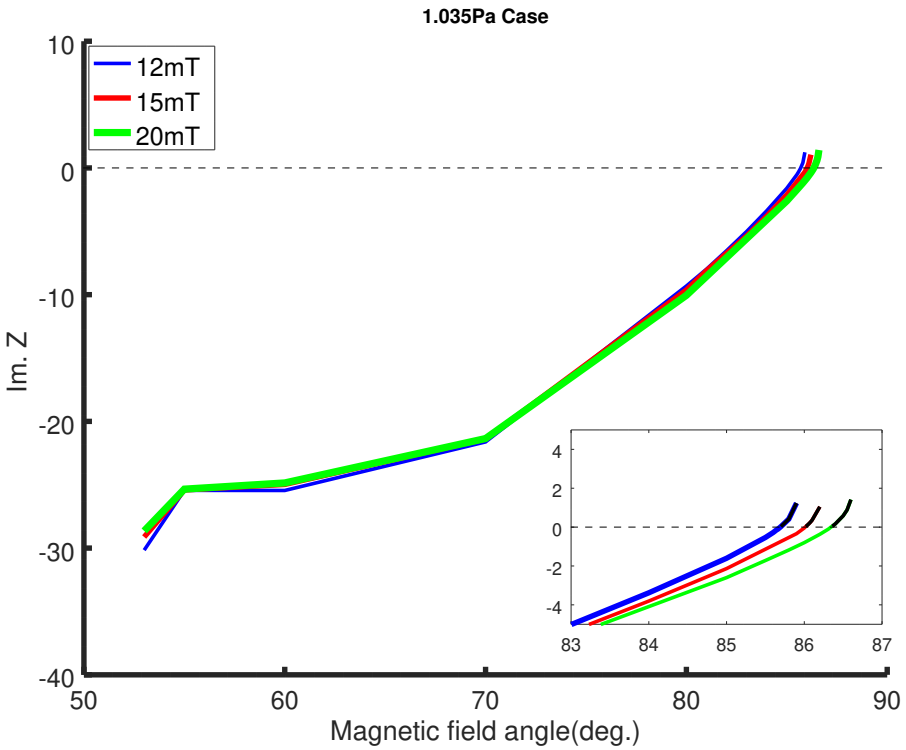

Figure 4.4: Variation of the imaginary impedance with magnetic field angle, for 1.035 Pa case, where positive imaginary impedance signifies a resonance, denoted by the black segments.

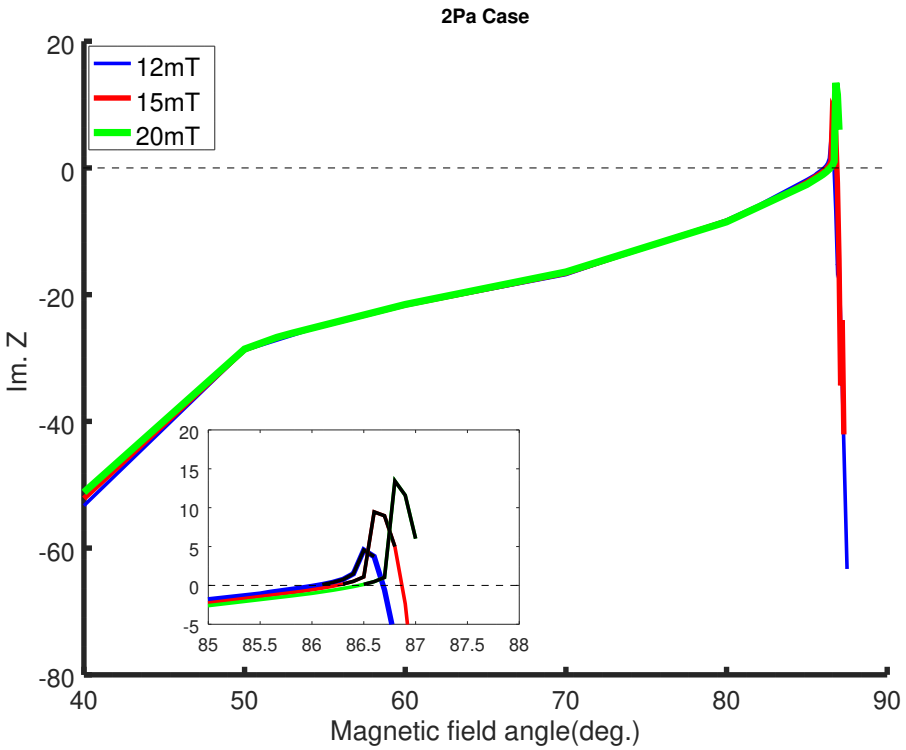

Figure 4.5: Variation of the imaginary impedance with magnetic field angle, for 2 Pa case, where positive imaginary impedance signifies a resonance, denoted by the black segments.

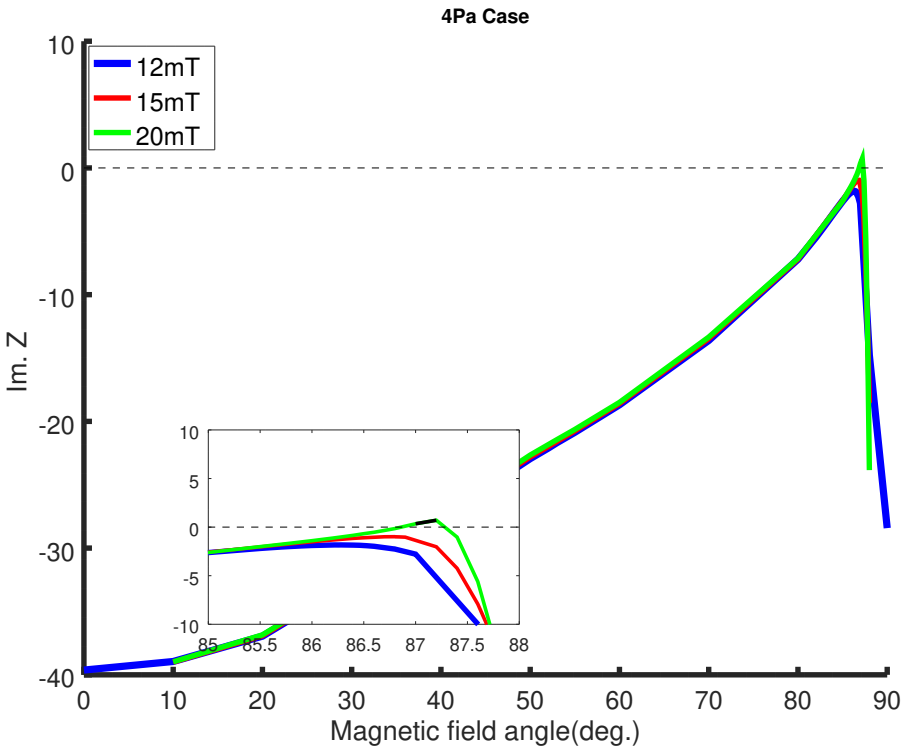

Figure 4.6: Variation of the imaginary impedance with magnetic field angle, for 4 Pa case, where positive imaginary impedance signifies a resonance, denoted by the black segments.

4.1.2 Ion Energy and Flux

Figures 4.7 and 4.8 shows the time-averaged ion energy and ion flux to the electrode over 1 RF cycle for the 1.035 and 2 Pa case, respectively. We are not including the 4 Pa case since the resonance effect is almost non-existent at this pressure. In both cases considered here, the ion flux increases while the ion energy decreases - they are coupled - which is expected in a single frequency CCP discharge. Once the resonance is reached, they begin to decouple - the ion flux begins to decrease while the ion energy continues to decrease. While this study constitutes a very narrow range, it appears that through the use of an oblique magnetic field to induce such resonances, it may be possible to achieve separate control of the ion flux and energy in single frequency, symmetric CCP discharges with further optimization i.e. identifying the paramaters to achieve maximum independant control.

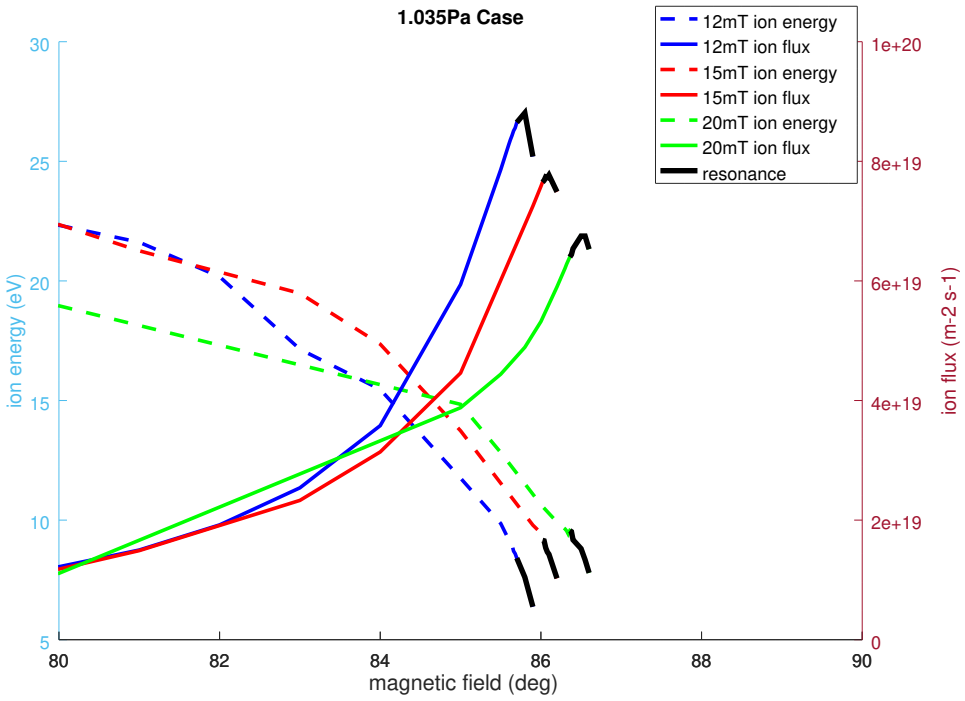

Figure 4.7: Ion energy and flux to the electrode as a function of magnetic field angle for 1.035 Pa at 12,15 and 20 mT field strengths. Black segments show the occurence of resonance while also highlighting the onset of the decoupling of the ion energy and flux.

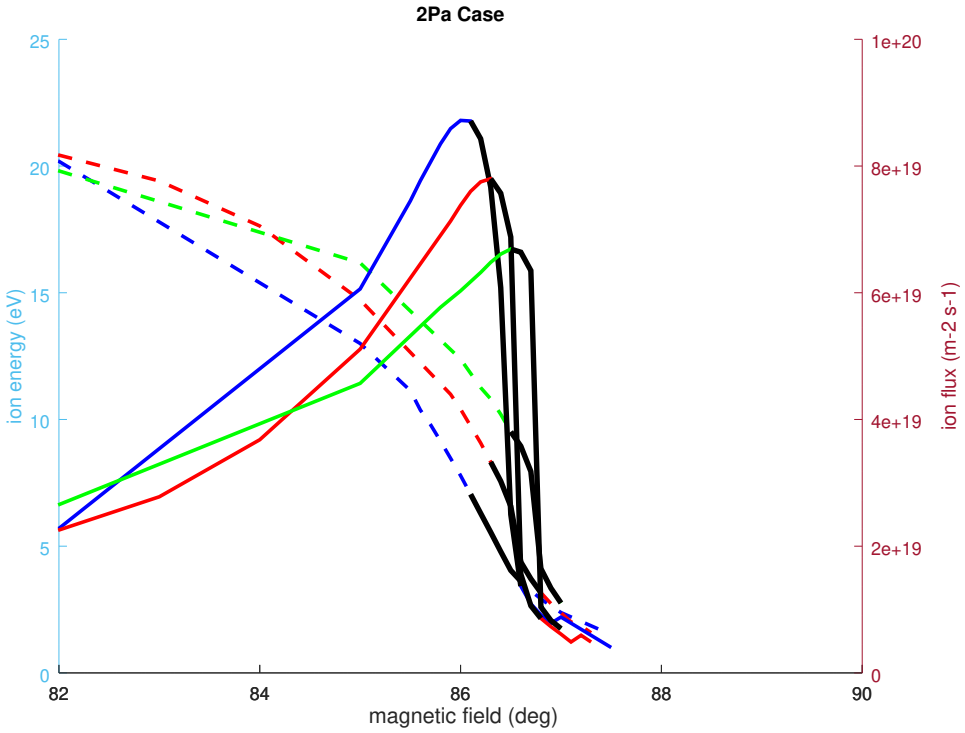

Figure 4.8: Ion energy and flux to the electrode as a function of magnetic field angle for 2 Pa at 12,15 and 20 mT field strengths. Black segments show the occurence of resonance while also highlighting the onset of the decoupling of the ion energy and flux.

4.1.3 Ion Energy Distribution Function

In plasma processing, the ion energy distribution function (IEDF) at the substrate is significant since it determines the etch rates and etch profiles in the etching processes as well as deposition rates and microstructures in deposition. IEDFs essentially describe the probability of ion impact at a surface for a given ion impact energy. As discussed in Section 3.2, ions are modulated by the RF sheath field and so the IEDF is determined mainly by the characteristics of the sheath[92]. The ability to control the IEDF is obviously advantageous in plasma processing and we are proposing the magnetized series resonance as a method to achieve this. We examined the IEDF at the powered electrode under both the presence and absence of the resonance condition for all cases as previously described in Section 4.1. It appears that the IEDF can be altered by the magnetized resonance in a single frequency CCP, while sensitive to pressure. While we found resonance for each pressure case, it appears that there is an increase in the population of higher energy ions compared to the situation where no resonance is present. However, this is more clearly seen for 2 and 4 Pa cases, Figure 4.10 and Figure 4.11 respectively, rather than 1.035 Pa case, Figure 4.9. Even though the resonance effect is less prominent at the 4 Pa case, it still suggests that the resonance induces a higher ion energy population. In conclusion, the use of the magnetized resonance phenomenon could provide be a method of tailoring the IEDF with further optimization.

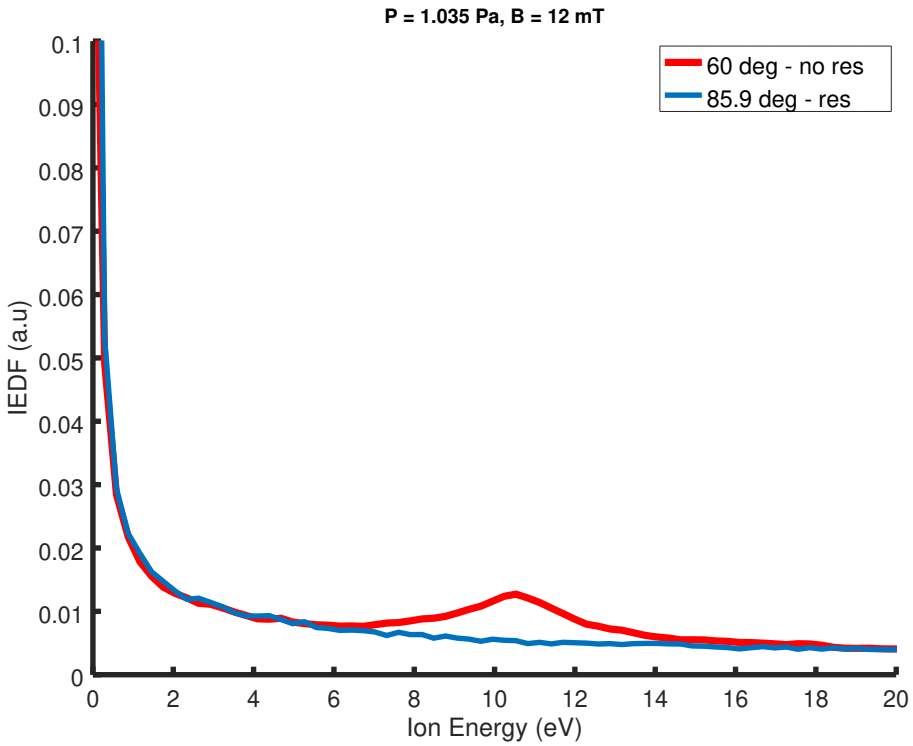

Figure 4.9: Comparison of IEDFs with and without the resonance at 1.035 Pa and 12 mT magnetic field.

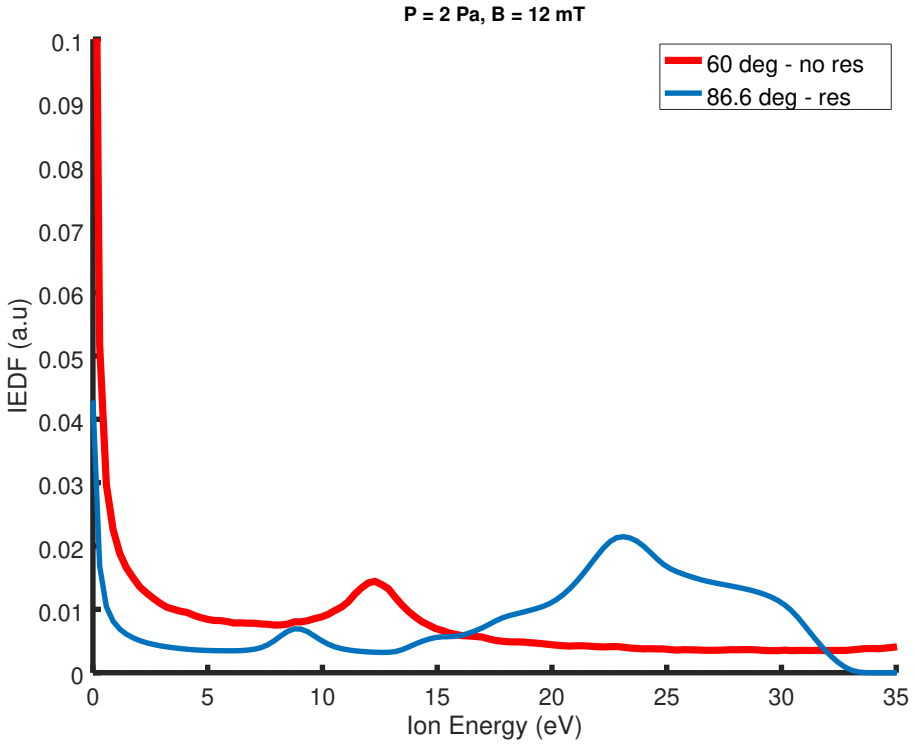

Figure 4.10: Comparison of IEDFs with and without the resonance at 2 Pa and 12 mT magnetic field.

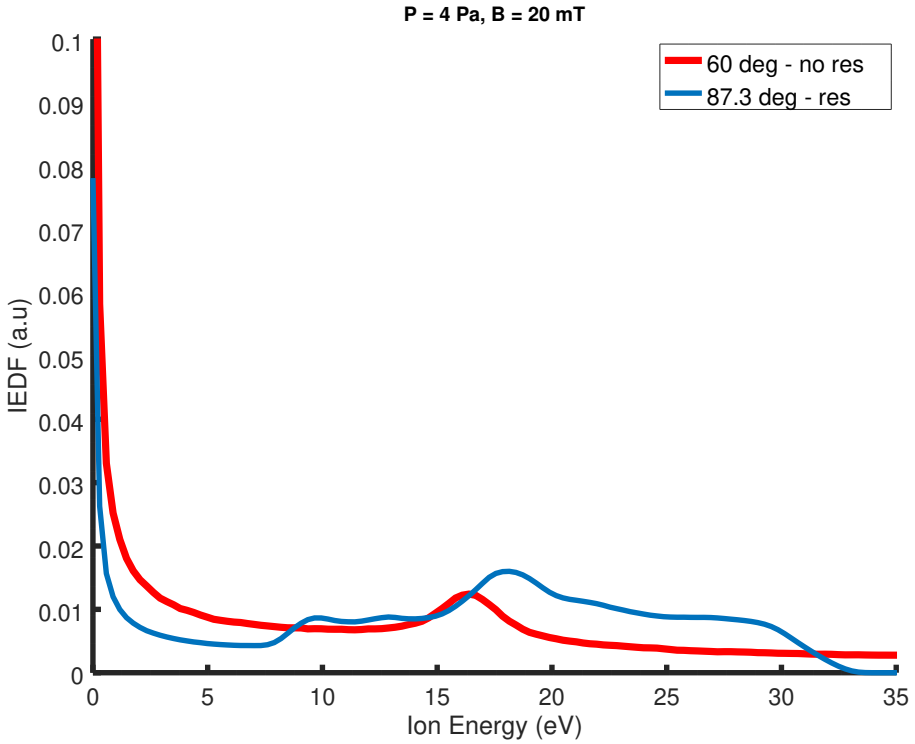

Figure 4.11: Comparison of IEDFs with and without the resonance at 4 Pa and 20 mT magnetic field.

4.1.4 Power Transfer

Power absorption is one of the key parameters that defines processes in any plasma source. In RF-CCP discharges power is transferred to the plasma by two mechanisms: (i) Ohmic (collisional) heating due to electron-neutral collisions and (ii) Stochastic (collisionless) heating whereby electrons collide with the oscillating sheath edge and gain energy from this collision. At low pressures, stochastic heating is the dominant mechanism for power transfer[45].

As mentioned earlier, we solve the power balance equation to determine the electron density. Graphically, this can be represented by plotting the plasma density versus the power absorbed by the electrons, as shown in Figure 4.12. The straight line represents the electron power loss and the curve represents the absorbed power. The intersection of this line with the curve indicates a stable solution i.e. the power absorbed perfectly cancels the power loss. Beyond this point, the power loss is greater than the power absorbed and a plasma cannot be sustained. This also supports our earlier observations, in Section 4.1.1, of a cut-off angle beyond which no stationary solutions can be found since these are both noted at the same value of θ.

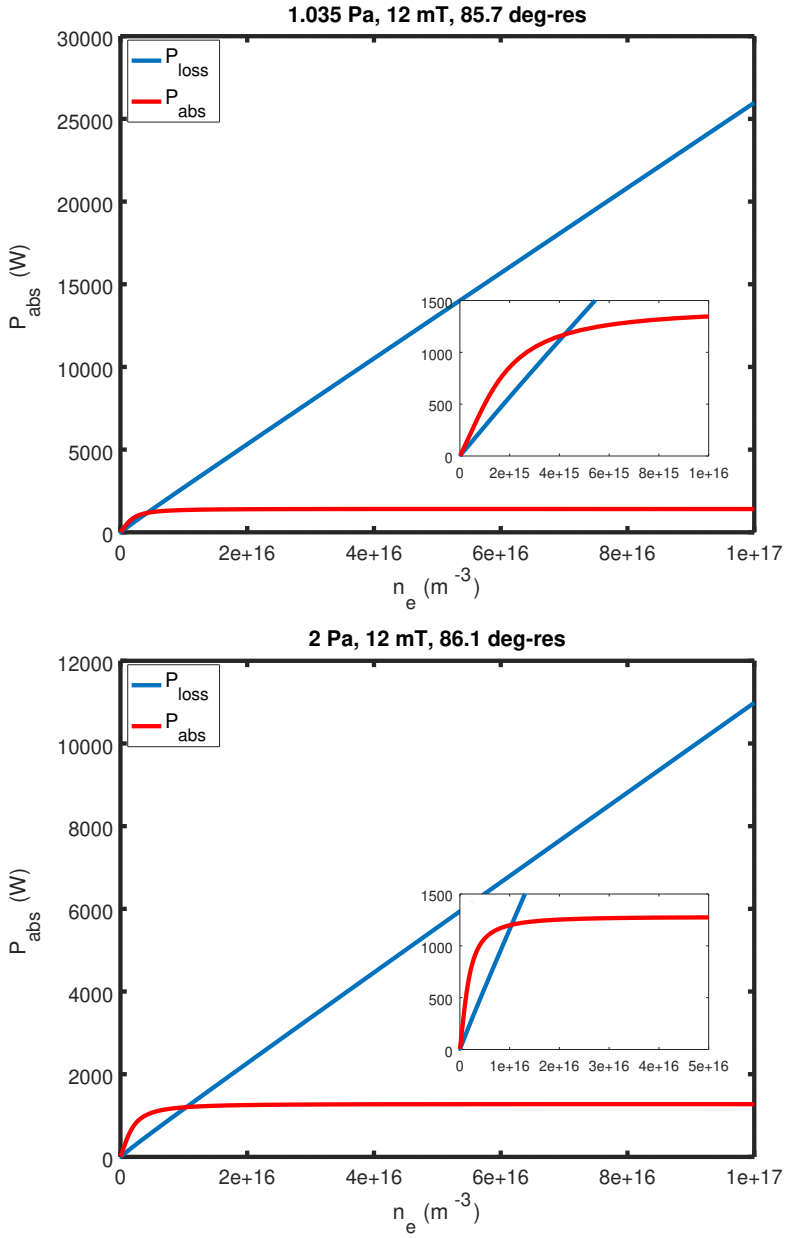

Figure 4.12: Absorbed power versus plasma density at resonance for a magnetic field strength of 12mT at (a) 1.035 Pa and $\theta = 85.7°$ and (b) 2 Pa and $\theta = 86.1°$. Red curve represents the power absorbed by the electrons, P_{abs}, while the blue line is the assumption of linear electron power loss, P_{loss}. The intersection of P_{abs} and P_{loss} indicates an equilibrium solution.

4.2 Conclusions

In this chapter we have introduced a possible method for independent control of ion energy and flux in single frequency CCP discharges, through the application of a magnetic field which induces a resonance effect. The occurrence of such a resonance is sensitive to the magnetic field orientation and for this study, only occurs for an extremely narrow range of angles. We have demonstrated within this narrow parameter range, the decoupling of the ion flux and energy, which may warrant applications in plasma processing. An advantage of our proposed method include the fact that it requires only a single frequency, and that frequency can be low so that electromagnetic effects are not an issue. Although, it does require the application of a magnetic field and some prior knowledge of the desired IEDF. Future work could focus on determining an optimized discharge configuration in order to improve control over the ion energy and flux.

CHAPTER 5

Sheath Models

In this chapter, we investigate how far conventional simple RF sheath models that do not consider a magnetic field, can be applied to the magnetized situation. First, we introduce some background theory on RF sheath models and highlight the need for such models. We then offer an insight into two such sheath models, Lieberman's sheath model and a sheath model put forward by Turner and Chabert, which is an extension of Lieberman's model. To this end, we have carried out a programme of 1D PIC simulations of an RF-CCP discharge in the presence of a variable angle magnetic field and compare these results with the models discussed in this chapter.

5.1 Introduction

Several types of models have been developed over the years, all with their own approach and assumptions, ranging from circuit models, analytical models, fluid models, kinetic models, and hybrid models. Godyak *et al*[93] offer a brief comparison of RF sheath models. Due to the complexity of sheaths, experimental measurements of this region have proven extremely difficult, so the use of sheath models can offer an alternative solution. Ultimately all models have the same goal - reduce the complexity in order to contribute to the understanding of sheath behaviour. Generally, RF sheaths are studied by employing the so-called "standard sheath model". This model assumes the RF regime where the applied frequency lies between the ion and electron plasma frequencies, i.e., $\omega_{pi} << \omega_{RF} << \omega_{pe}$, and also imposes the length scale ordering $\lambda_D << s_m << L$. In the following sections, we briefly introduce some simple sheath models that do not consider a magnetic field.

5.2 Ion Matrix sheath model

In a situation where the sheath voltage is very large compared to the electron temperature, the electron population in the sheath can be neglected, and only the ions are considered. This simple model of a high-voltage sheath assumes a uniform ion density within the sheath, i.e., homogeneously distributed throughout the sheath, so $n_i = n_s = constant$, where n_i is the ion density in the bulk and n_s is the ion density at the sheath edge. This type of sheath is known as a matrix sheath with a thickness, s, given by:

$$s = \left(\frac{2\epsilon_0 V_0}{e n_s} \right) \tag{5.1}$$

where V_0 is the sheath voltage. Matrix sheath models are generally useful when considering the situation where the mobility of ions is limited in the sheath i.e. at high pressures. This model is considered one of the most simplistic sheath models.

5.3 Child Sheath Model

The Child-Langmuir model[94][95] offers a more accurate representation of a high-voltage sheath compared to the ion matrix sheath model since it takes into account the decrease in ion density due to their acceleration across the sheath. In this model, the plasma consists of singly charged ions and electrons, and the sheath is completely devoid of electrons, while the ion motion is assumed collisionless. The boundary conditions imposed in this model require ions to enter the sheath with zero velocity, and the electric field is also zero at the plasma-sheath edge. The Child-Langmuir law relates the voltage drop across the sheath V, the sheath thickness s, and ion current density J, through the sheath by the following equation:

$$J = \frac{4\epsilon}{9}\sqrt{\frac{2e}{m_e}}\frac{V^{\frac{3}{2}}}{s^2} \tag{5.2}$$

The Child sheath width is larger compared to the matrix sheath width due to the fact it considers the decreasing ion density in the sheath. This model is most accurate for cases when the sheath voltage is very highly negative with respect to the plasma potential since electrons will be fully repelled from the sheath region[96].

5.4 Lieberman Model

Lieberman[97] provides an analytical model for a capacitive RF sheath driven by a single frequency sinusoidal RF current source from which the time-averaged plasma parameters can be determined. It is assumed ions enter the sheath with the Bohm velocity, v_B, and that their motion within the sheath is collisionless. The ions respond only to the time-average electric field while the electrons respond to the instantaneous electric field. Lieberman uses a step model for the electrons, assuming the electron density drops sharply from $n_e \approx n_i$ on the plasma side of the electron sheath to $n_e \approx 0$ on the electrode side. The electron sheath oscillates during the RF cycle between a maximum and minimum sheath width. Lieberman derives the fundamental equations of the RF sheath given by Eq. 5.3 and Eq. 5.4:

$$\frac{d\bar{\Phi}}{dx} = -\frac{\tilde{J}_0}{\epsilon_0 \omega \pi}(\sin\phi - \phi\cos\phi) \tag{5.3}$$

$$\frac{d\phi}{dx} = \frac{(1 - 2\bar{\Phi}/T_e)^{-1/2}}{\tilde{s_0}\sin\phi} \tag{5.4}$$

where $\bar{\Phi}$ is the time-average potential within the sheath, $\tilde{J}_0$ is the current density, $\phi = \omega t$, $\tilde{s_0}$ is the sheath oscillation amplitude given by $\tilde{s_0} = \tilde{J}_0/e\omega n_0$. From these equations Lieberman expresses the sheath quantities as a function of a single dimensionless parameter H, given by Eq. 5.5.

$$H = \frac{\tilde{J_0}^2}{e n_0 \pi \epsilon_0 \omega^2 k_B T_e} \tag{5.5}$$

A limitation of this model is the exclusion of electron particle current to the electrode. The use of a step model can restrict application since it fails when

$V_{RF} >> k_B T_e/e$ is not met and since it considers the electric field in the sheath, and not in the plasma, raises an issue with boundary conditions.

5.5 Turner-Chabert Model

One of the limitations of Lieberman's model is the fact it deals with an RF sheath excited by a single frequency only, which is not applicable to many modern-day experiments. Turner and Chabert[98] present a simple RF sheath model that can be solved for arbitrary excitation waveforms that still agrees with Lieberman's model for single frequency excitation. Their model is a simplification of Lieberman's using the ansatz that the time-averaged electron density is a constant fraction of the ion density, represented by Eq. 5.6. This introduces an appropriate amount of electron space charge but approximates the spatial distribution of this charge.

$$\bar{n}_e = (1 - \xi) n_i \tag{5.6}$$

where

$$\xi = \frac{\bar{V}}{V_0} \tag{5.7}$$

$\bar{n}_e$ is the time-averaged electron density, n_i is the ion density, $\bar{V}$ is the time-averaged sheath voltage and V_0 is the maximum sheath voltage. By use of this approximation, it allows the treatment of arbitrary excitation waveforms without affecting the accuracy of the model. Cases for dual-frequency and pulse-like waveforms are considered, and it is shown that the error introduced by this approximation is small.

5.6 Simulation Results

The following simulation results are based on the parameters described in Chapter 4, summarized in Table 4.1. We compare sheath voltages, ion currents and sheath widths from our simulations with model predictions to determine it's applicability in describing the magnetized situation. Our data is obtained by changing the magnetic field angle and calculating the parameters mentioned above for each value of θ. We expect magnetized electrons, unmagnetized ions, and weak collisional effects in the sheath. For each case, we compare our simulation results to the model predictions to see how far the model can hold for different magnetic field strengths and magnetic field angles. The ability to describe the complicated situation of a magnetized sheath with a simple model would prove useful in terms of modeling.

5.6.1 Comparison of voltages

The maximum sheath voltage, V_0, and mean sheath voltage, $\bar{V}$, according to the model are given by:

$$V_0 = \frac{2J_0 s_m}{K_{cap}\omega\epsilon_0} \tag{5.8}$$

$$\bar{V} = \xi V_0 \tag{5.9}$$

where J_0 is the current density, s_m is the sheath width and K_{cap} is a dimensionless parameter given by K_{cap}= 4/3.

Again, we consider the three different pressure cases (1.035, 2, and 4 Pa), where the magnetic field strength is varied as we scan the magnetic field angle, θ. We plot the magnetic field angle as a function of H given by Eq.5.5. A similar trend is observed in all cases. In general, for $\theta < 80°$, the model and simulation data agree well, with the model predicting slightly higher sheath voltages. For $\theta > 80°$, there is a dramatic shift in the sheath voltages, with both the model and simulations predicting this shift, as can be seen in Figures 5.1 - 5.3. However, it is more prominent for the 2 and 4 Pa cases. It appears that for angles greater than 80°, there is a dramatic drop in the sheath voltage as the magnetic field becomes more oblique, even under the exotic circumstances where the resonance is present. As a result, we can conclude that this simple model has the ability to describe the magnetized situation quite well.

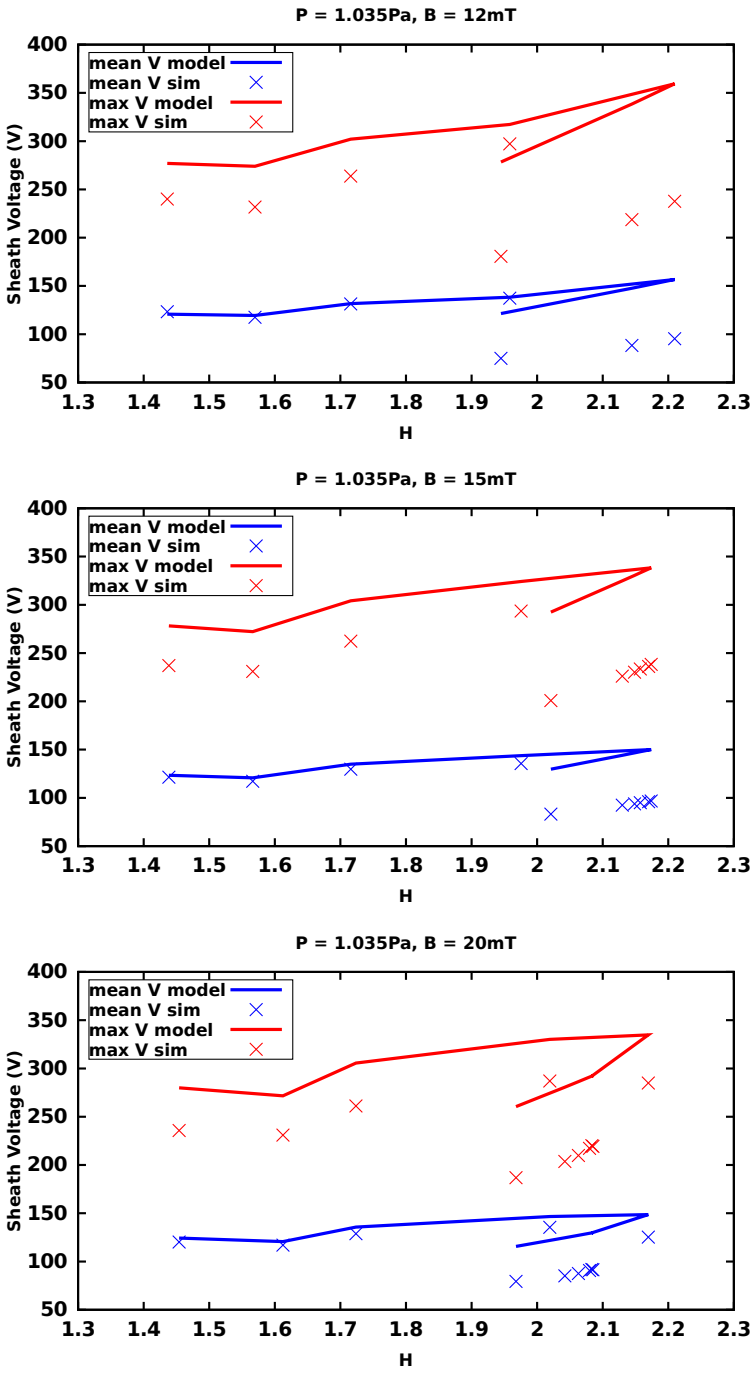

Figure 5.1: Comparison of sheath voltages from simulation and model predictions. Points represent the simulation data while the solid line presents the model predictions for maximum(red) and mean(blue) sheath voltages. For 3 different magnetic field strengths: 12mT (top), 15mT (middle) and 20mT(bottom) at 1.035Pa.

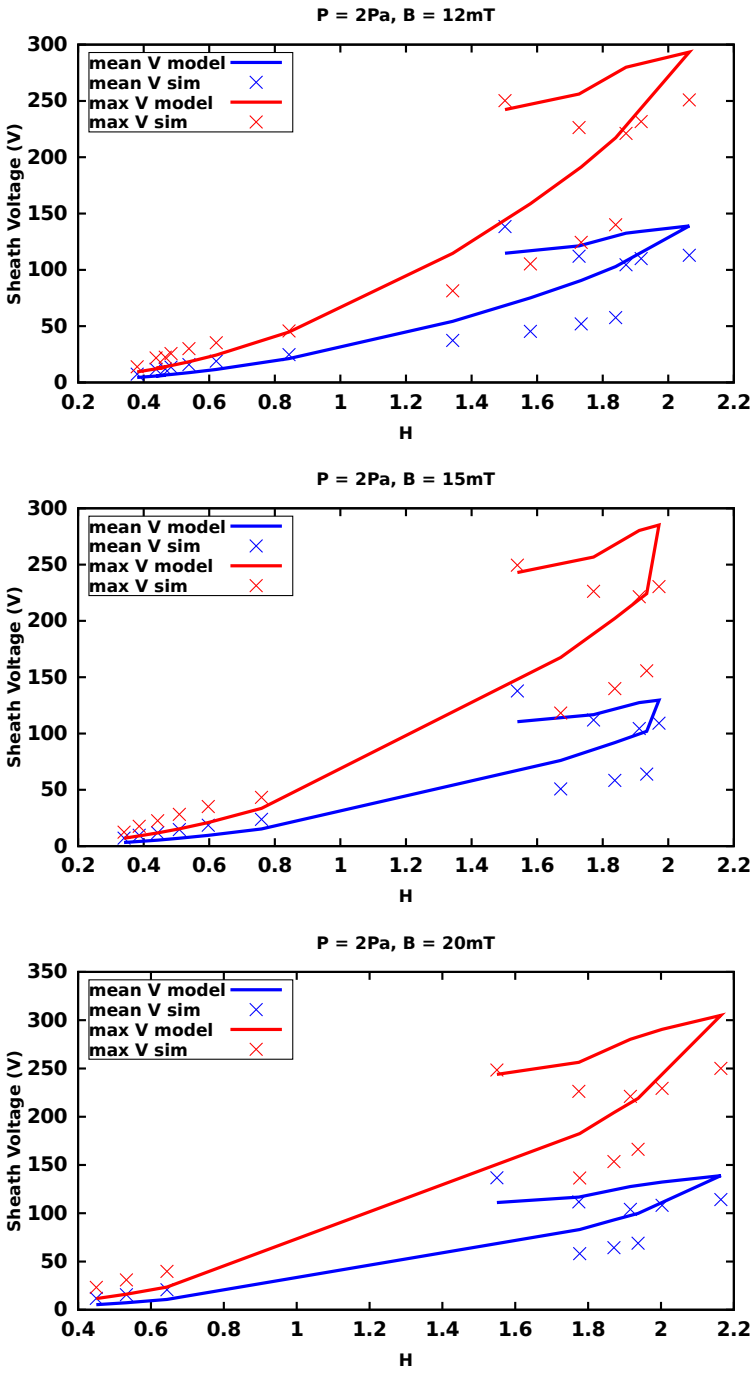

Figure 5.2: Comparison of sheath voltages from simulation and model predictions. Points represent the simulation data while the solid line presents the model predictions for maximum(red) and mean(blue) sheath voltages. For 3 different magnetic field strengths: 12mT (top), 15mT (middle) and 20mT(bottom) at 2Pa.

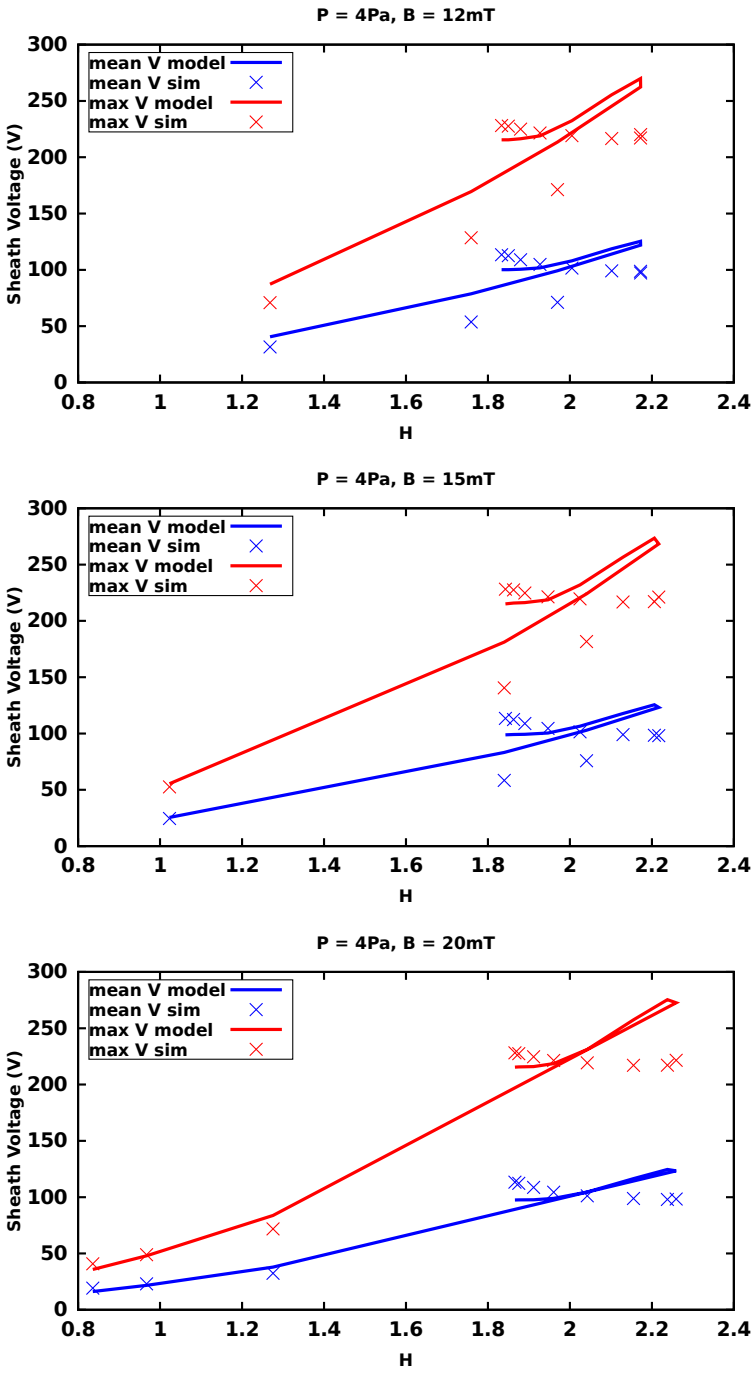

Figure 5.3: Comparison of sheath voltages from simulation and model predictions. Points represent the simulation data while the solid line presents the model predictions for maximum(red) and mean(blue) sheath voltages. For 3 different magnetic field strengths: 12mT (top), 15mT (middle) and 20mT(bottom) at 4Pa.

5.6.2 Comparison of currents

Next, we compare the ion current in the simulation with the prediction of the model to further test its applicability. The ion current in the model is given by:

$$J_i = K_i \frac{\epsilon_0}{s_m^2} \left(\frac{2q_e}{m_i} \right)^{\frac{1}{2}} (\xi V_0)^{\frac{3}{2}} \tag{5.10}$$

where $K_i = 4/9\xi$. Figures 5.4-5.6 show the comparison between the model predictions and simulation results. For the lowest pressure, the model and simulation agree reasonably well up to and including resonance occurring, less so as we increased the magnetic field strength, see Figure 5.4. Increasing the pressure (2 Pa), we can see a deviation between the model and simulation results for the angles where resonance occurs, Figure 5.5. At this point, one could almost suggest that the model cannot be applied when resonance is present. However, when we further increase the pressure (4 Pa), it is realised that it is not the resonance that the model cannot describe, but rather angles $\theta \geq 87°$, i.e., grazing angles with the plates. For the 4 Pa case, simulations found no resonance for the 12mT case and 15mT case despite considering a range of angles up to and including $\theta = 87°$, For instance, for 12mT case $\theta = 87°$ represents the point where the simulation and model are visibly diverging, Figure 5.6 (top), and for the 15mT case similar situation occurs for $\theta = 87.2°$, Figure 5.6 (middle). Whereas, for the 20mT case, we found resonance at $\theta = 87, 87.2, 87.3°$. We do not see this deviation in the lowest pressure case since resonance occurs for $\theta < 87°$. As a result, we can conclude that while the model may be applied to the magnetized situation, it may be limited when it comes to describing grazing angles with the plates.

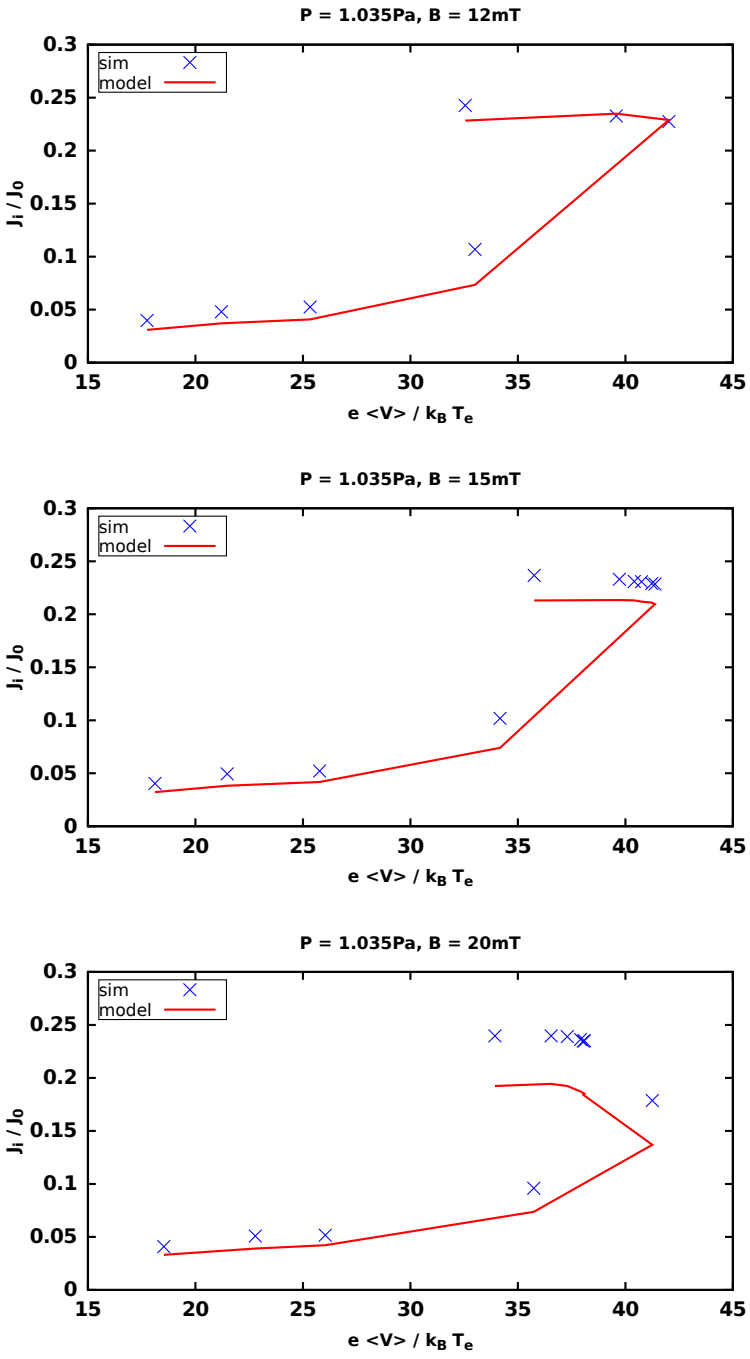

Figure 5.4: Comparison of ion current in the simulation with model predictions. Points represent the simulation data while the solid line presents the model predictions for 3 different magnetic field strengths: 12mT (top), 15mT (middle) and 20mT(bottom) at 1.035 Pa.

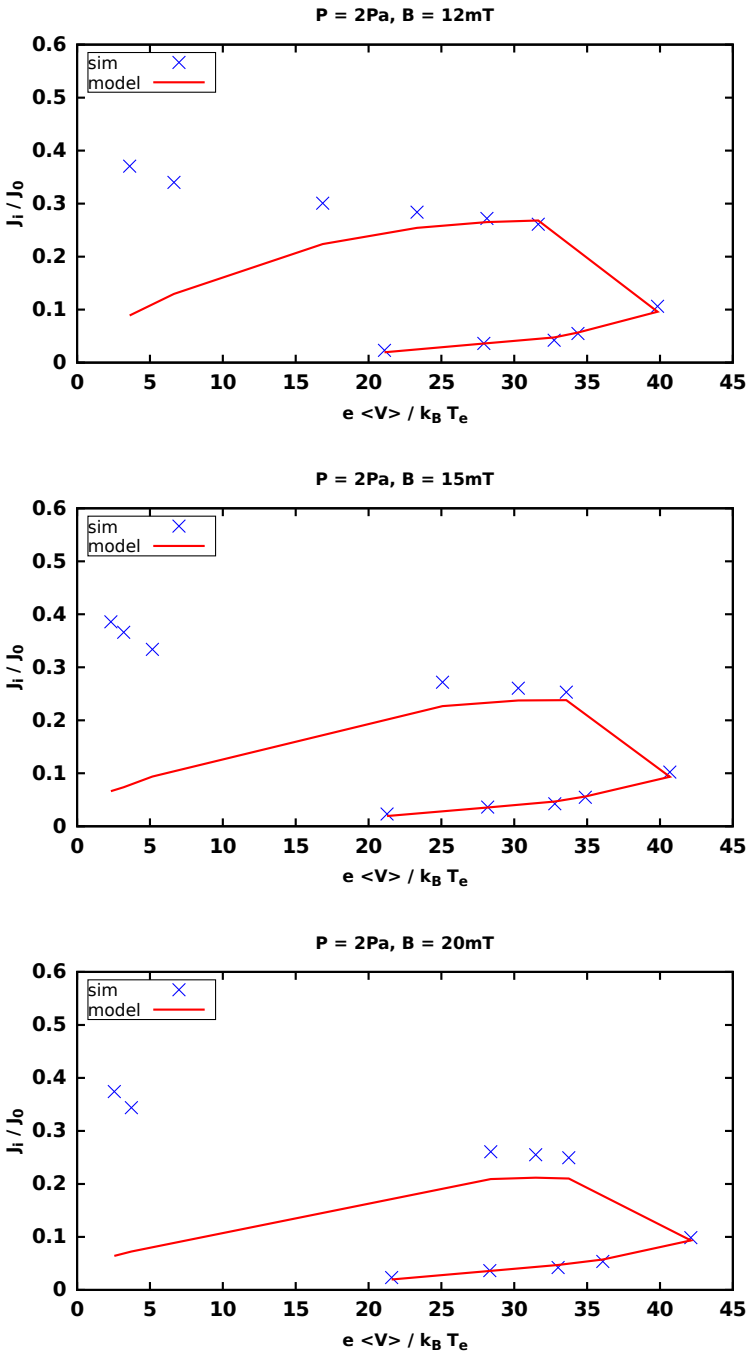

Figure 5.5: Comparison of ion current in the simulation with model predictions. Points represent the simulation data while the solid line presents the model predictions for 3 different magnetic field strengths: 12mT (top), 15mT (middle) and 20mT(bottom) at 2 Pa.

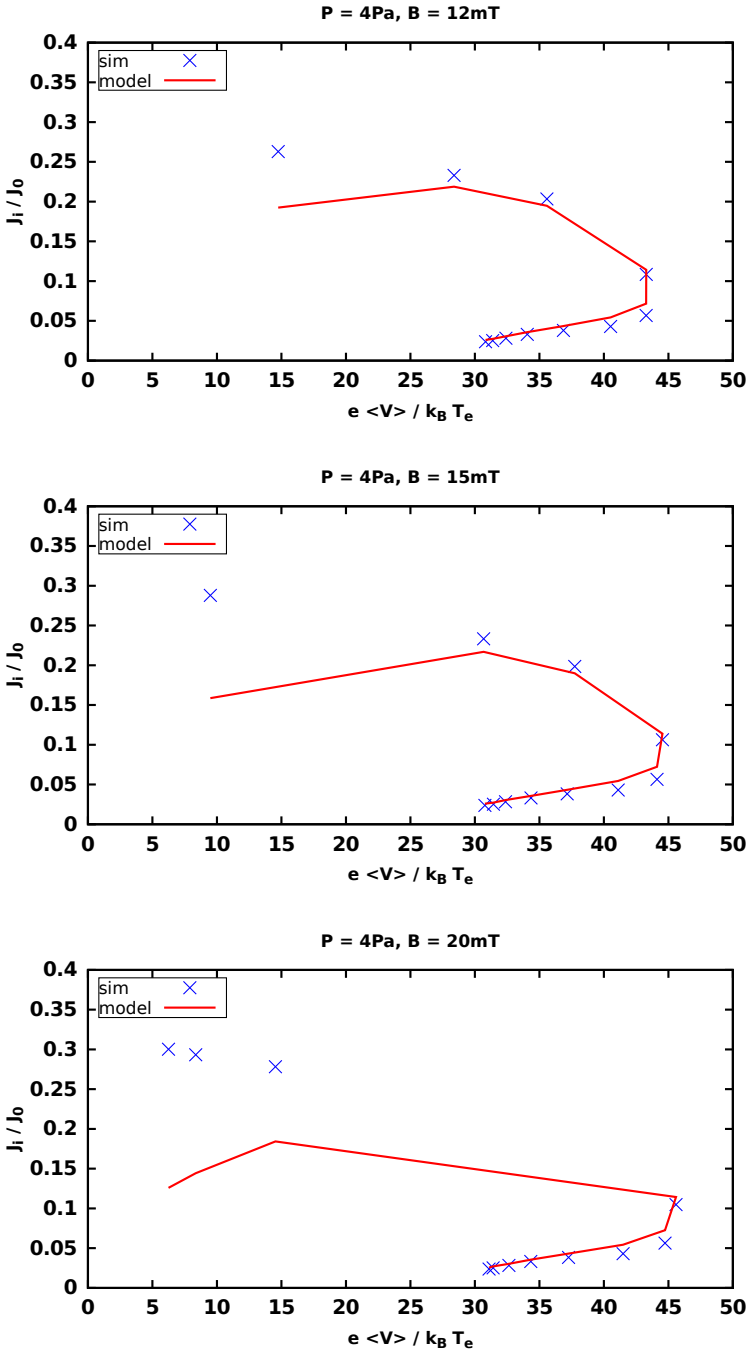

Figure 5.6: Comparison of ion current in the simulation with model predictions. Points represent the simulation data while the solid line presents the model predictions for 3 different magnetic field strengths: 12mT (top), 15mT (middle) and 20mT(bottom) at 4 Pa.

5.6.3 Comparison of sheath width

From the model the sheath width is given by:

$$s_m = \frac{K_s J_0^3}{q_e \epsilon_0 k_B T \omega^3 n_0^2} \tag{5.11}$$

with $K_s = 4\xi/3$. As discussed in Section 2.3.6, we consider three different definitions of the sheath edge location. Therefore we offer a comparison of each of these definitions with the sheath width predicted by the model. Recalling these definitions as the following:

1. Charge Compensation(CC): The point where the positive space charge in the sheath, n_+, exactly compensates the negative surface charge, $-\sigma$, and the electric field is zero:

$$\int_{electrode}^{sheathedge} n_+(x)dx = -\sigma \tag{5.12}$$

2. Bohm Condition(BC): The point at which ions reach the Bohm velocity:

$$u_B = \sqrt{\frac{kT_e}{m_i}} \tag{5.13}$$

3. Ion Current(IC): Using the sheath edge ion density, n_s, implied by the ion current, J_i, to determine the sheath edge:

$$J_i = en_s u_B \tag{5.14}$$

For the 1.035 Pa case, while the model and simulation differ slightly, they both still predict a decreasing sheath width as the angle with the plates becomes more shallow, with the model predicting a smaller sheath width overall for all three definitions, as can be seen in Figure 5.7. Also, both the simulations and model predict a rapidly varying sheath width according to the BC sheath definition as the angle becomes very shallow. For the 2 Pa case, we see a better agreement between the simulation data and model predictions. However, the model predicts a sheath collapse, for each definition of the sheath width, where resonance occurs, shown in Figure 5.8. While for the 4 Pa case, no resonance is found for the 12 mT and 15 mT case, the model predicts smaller sheath values than the simulations. For the 20 mT case, where resonance occurs for $\theta = 87, 87.2, 87.3^\circ$ again, the model predicts a sheath collapse, Figure 5.9. As a result, from this comparison, we determine that while the model offers reasonable predictions for sheath width in this magnetized situation, it appears to be less dependable in the presence of resonance.

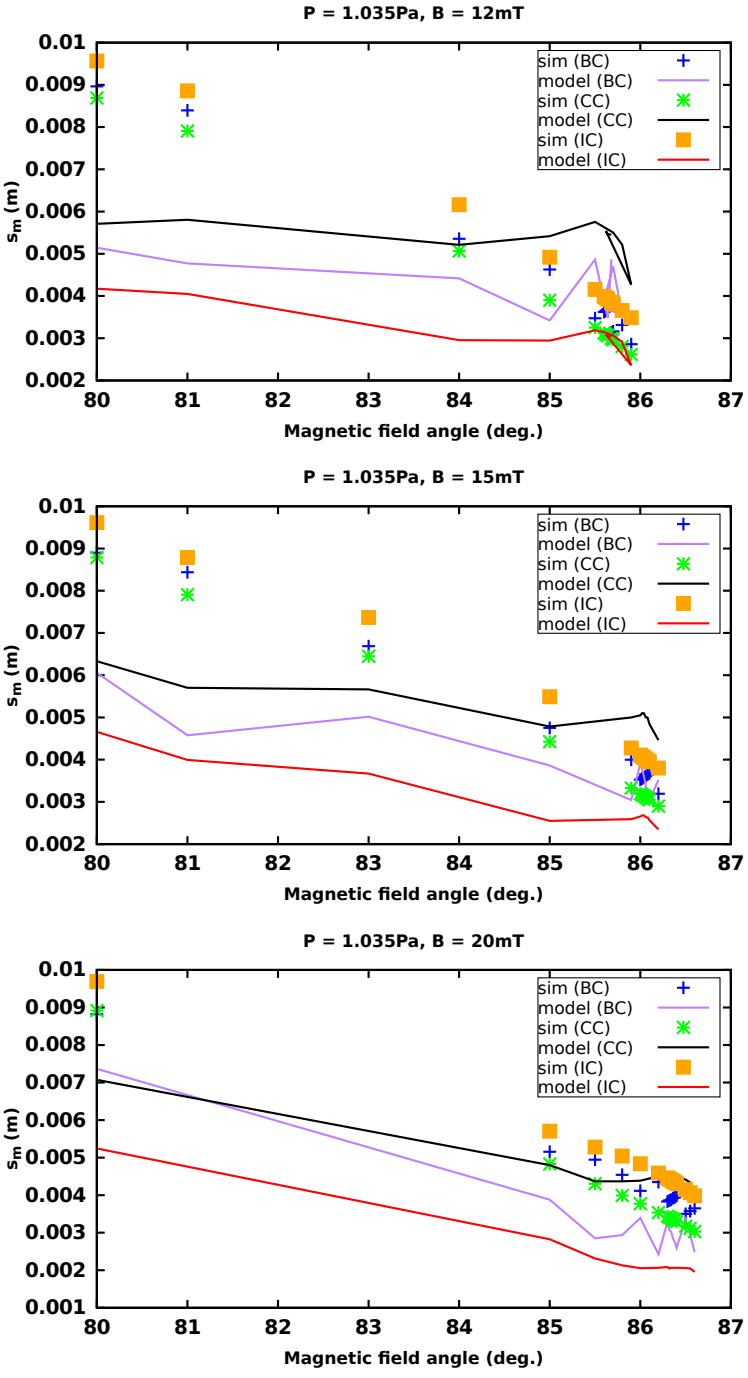

Figure 5.7: Comparison of sheath widths from simulations with model predictions. Points represent the simulation data while the solid line presents the model predictions for 3 different magnetic field strengths: 12mT (top), 15mT (middle) and 20mT(bottom) at 1.035 Pa.

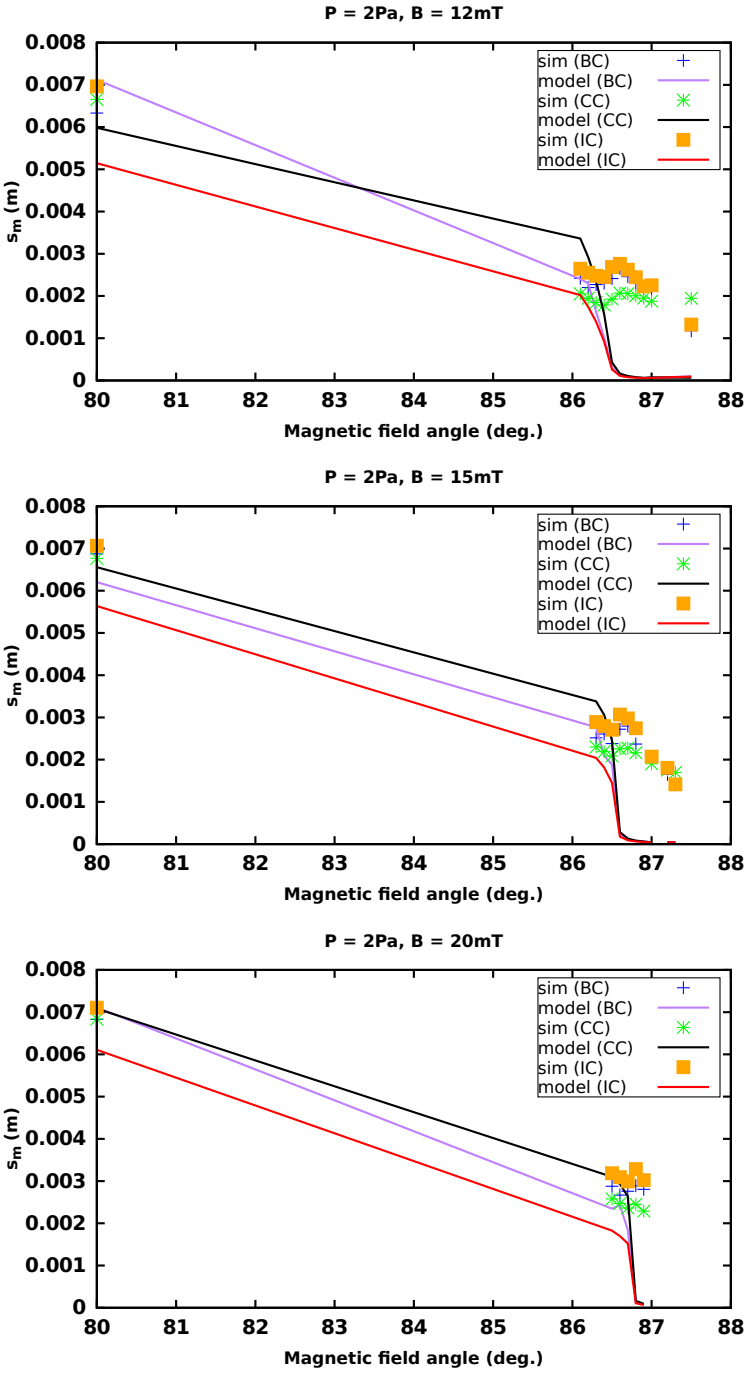

Figure 5.8: Comparison of sheath widths from simulations with model predictions. Points represent the simulation data while the solid line presents the model predictions for 3 different magnetic field strengths: 12mT (top), 15mT (middle) and 20mT(bottom) at 2 Pa.

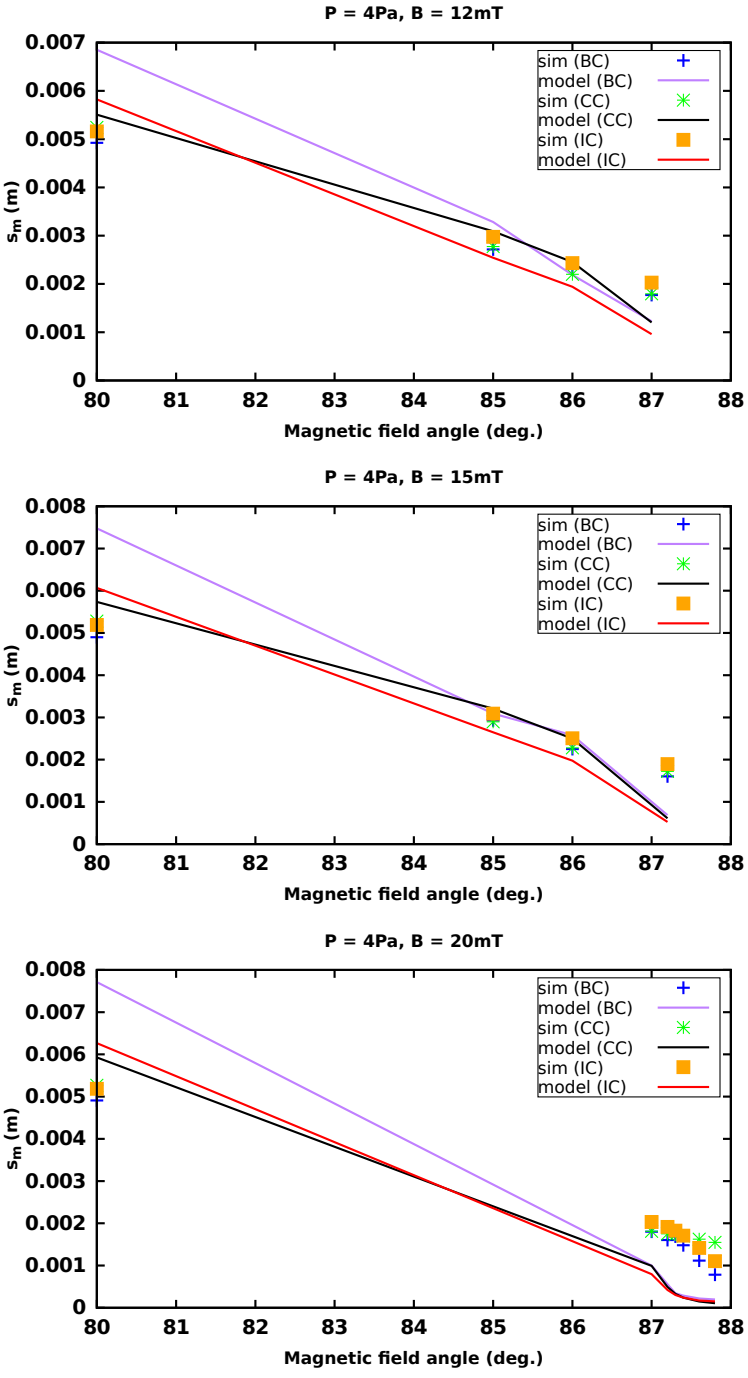

Figure 5.9: Comparison of sheath widths from simulations with model predictions. Points represent the simulation data while the solid line presents the model predictions for 3 different magnetic field strengths: 12mT (top), 15mT (middle) and 20mT(bottom) at 4 Pa.

5.7 Conclusions

Following the comparison of this simple model with our simulation results, based on predictions of (i) sheath voltages (ii) ion currents and (iii) sheath widths, we can conclude that this simple sheath model appears adequate to describe the magnetized situation, but it has limits. The presence of the magnetic field has made no appreciable difference to the model predictions provided $\theta < 80°$. Therefore, it appears that RF sheaths can be adequately described by simple models (that ignore the magnetic field), in the presence of an oblique magnetic field, but less so for grazing magnetic field angles or exotic circumstances such as resonance. We arrive at this conclusion due to the fact that for the current comparison study, the discrepancies between model and simulation occurred for $\theta > 87°$, regardless if resonance is present or not. While for the sheath width comparisons, the discrepancies appear to be directly linked to the resonance. This suggests that the use of such simple models as sheath boundary conditions for models that consider the entire device may prove useful.

CHAPTER 6

Experiment and Simulation Study

6.1 Experimental Work

This chapter includes experimental work provided by a collaboration with the group at the Institute of Plasma Research (IPR), Gandhinagar, Gujarat, India, to further enhance our study of magnetized sheaths in RF-CCP discharges. As we have emphasized, simulations have become an indispensable tool in plasma physics research. However, one must remember that simulations are imperfect models, and in a sense, can only be deemed reliable in conjunction with experimental results. At the same time, experimental results are known to be subject to significant uncertainties and errors[99]. In this sense, simulations and experiments can be seen as complementary to one another, which was the goal of this collaboration.

6.1.1 Experimental Setup

The RF-CCP experimental setup consists of two rectangular plates, 10 cm wide and 40 cm long, housed in a cylindrical glass vacuum chamber that is evacuated by a turbo molecular pump and a mechanical backing pump. The distance between the plates can be varied between 2-8 cm and they can be rotated so to have different angles with the magnetic field. For the experimental results presented throughout this chapter the magnetic field is kept parallel to the plates and the plate separation is fixed at 8 cm. The magnetic field is generated by a pair of electromagnet coils and is uniform along the length and width of the discharge, with a maximum achievable field strength of 50 mT. The RF voltage is driven at a frequency of 13.56 MHz for this experiment. The plates are capacitively driven in a push-pull configuration using a 1:1 center-tap ferrite transformer. The center tap 1:1 transformer was designed to give the floating RF voltage to the electrodes. Instead of giving +/- to one plate and ground to other plate, +/- will be provided to both plates, but 180 degrees out of phase and the ground (zero) will be at the center of the discharge. When dealing with an RF power supply extra attention is needed regarding grounding. The RF power supply and the match box are grounded through high value of inductor. The inductors are placed in the ground path to block RF component and allow only DC to pass through. The inductor is made with a ferrite core with a winding of Teflon coated wire[100][6]. The experimental setup is depicted in detail in Figures 6.1 and 6.2.

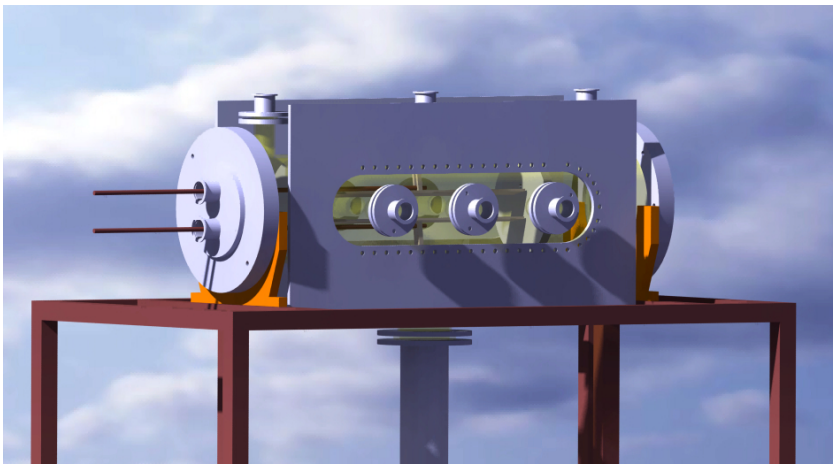

Figure 6.1: Schematic of the experimental setup of RF-CCP system provided by the group at IPR, India.

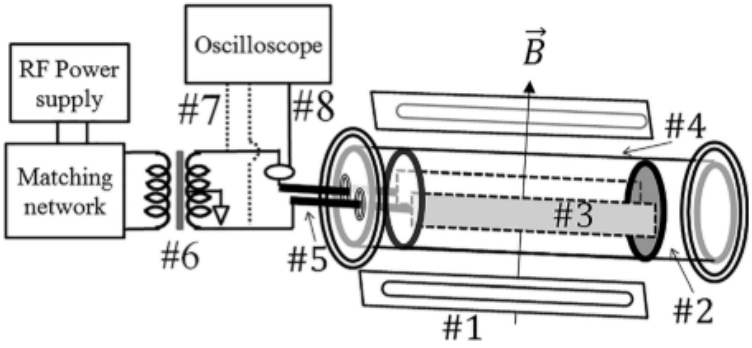

Figure 6.2: Schematic of the experimental setup of RF-CCP system taken from [6]. 1: Electromagnetic coils, 2: Teflon support, 3: SS parallel plates, 4: glass chamber, 5: high voltage copper feedthrough, 6: ferrite transformer, 7: voltage probes, and 8: current transformer.

6.1.2 Experimental Diagnostics

Temperature is among one of the most important parameters of a plasma and so we focused on obtaining a comparison between simulation and experimental measurements. For the experiment, an emissive probe was applied along the center of discharge to obtain a spatially resolved measurement of the electron temperature, T_e. The probe consists of a tungsten filament which measures floating potential when cold and measures the potential very close to the plasma when heated sufficiently[101]. The electron temperature is calculated using the floating, V_f, and plasma potential, V_p, since the difference between them provides sufficient potential that is responsible for the velocity of the electrons. As a result, the following equation was used to determine the electron temperature:

$$V_p - V_f = T_e \ln \left(\frac{m_i}{2\pi m_e} \right)^{1/2} \tag{6.1}$$

The probe is pushed into the center of the plasma through a fine slit on the top electrode. The first measurement was taken at 0.5 cm away from the electrode, while the rest of the readings were taken at an interval of 1 cm, overall scanning a total of 6.5 cm.

6.1.3 Experimental Results

The experiments considered two cases : (i) no magnetic field and (ii) a parallel magnetic field, at two different pressures, 1 and 4 Pa. The working gas was chosen to be Argon. The plate separation was kept constant at 8 cm for both cases. Voltages of approximately 50-60 V were obtained for magnetized case, and 200 V for non-magnetized case. For obtaining the discharge voltage, the voltage between the two plates was measured using a textronix voltage probe. While the current is measured using a current transformer placed at one of the coaxial line going to discharge plate. All discharge voltage and current are RMS values. For the magnetized cases, a parallel magnetic field of 7 mT is applied and electrons can be assumed to be weakly magnetized while the ions are not. The power going into to plasma was calculated by

$$P = V_{rms} I_{rms} \cos\theta \tag{6.2}$$

where θ is phase between voltage and current. It was necessary to calculate the power in this way since it was found, especially for the magnetized case, that the RF generator experienced high reflection and often did not give correct readings. For example, for a set power of 20 W, it was found that only 11 W was actually being transferred to the discharge.

6.1.3.1 No Magnetic Field

The first experiment involved the measurement of T_e in an un-magnetized discharge at 1 and 4 Pa. It was found that T_e appears to remain constant throughout the bulk with a sharp increase near the plates as shown in Figure 6.3. The increase in T_e near the plates is attributed to the fact that stochastic heating is dominant near the sheaths while ohmic heating is dominant in the bulk. This trend is similar for both 1 and 4 Pa cases, with an overall reduced temperature in the 4 Pa case which is expected with increasing pressure, due to the higher collisionality.

6.1.3.2 Parallel Magnetic Field

A magnetic field of 7mT is applied parallel to the plates, such that the electrons can be considered weakly magnetized while the ions are not. The presence of the magnetic field results in an inhomogeneous plasma. A step-like density profile between the plates was observed experimentally, which was attributed to the $E \times B$ drift motion of electrons in the bulk plasma. In the presence of the parallel magnetic field, T_e exhibits a V-shaped profile resulting from a falling trend from near sheath regions to the center of the discharge. When the pressure is increased this profile gets slightly skewed, as can be seen in Figure 6.5. This indicates that the discharge is not uniform in the bulk due to drifts of charged particles and this drift is further hindered as the pressure is increased.

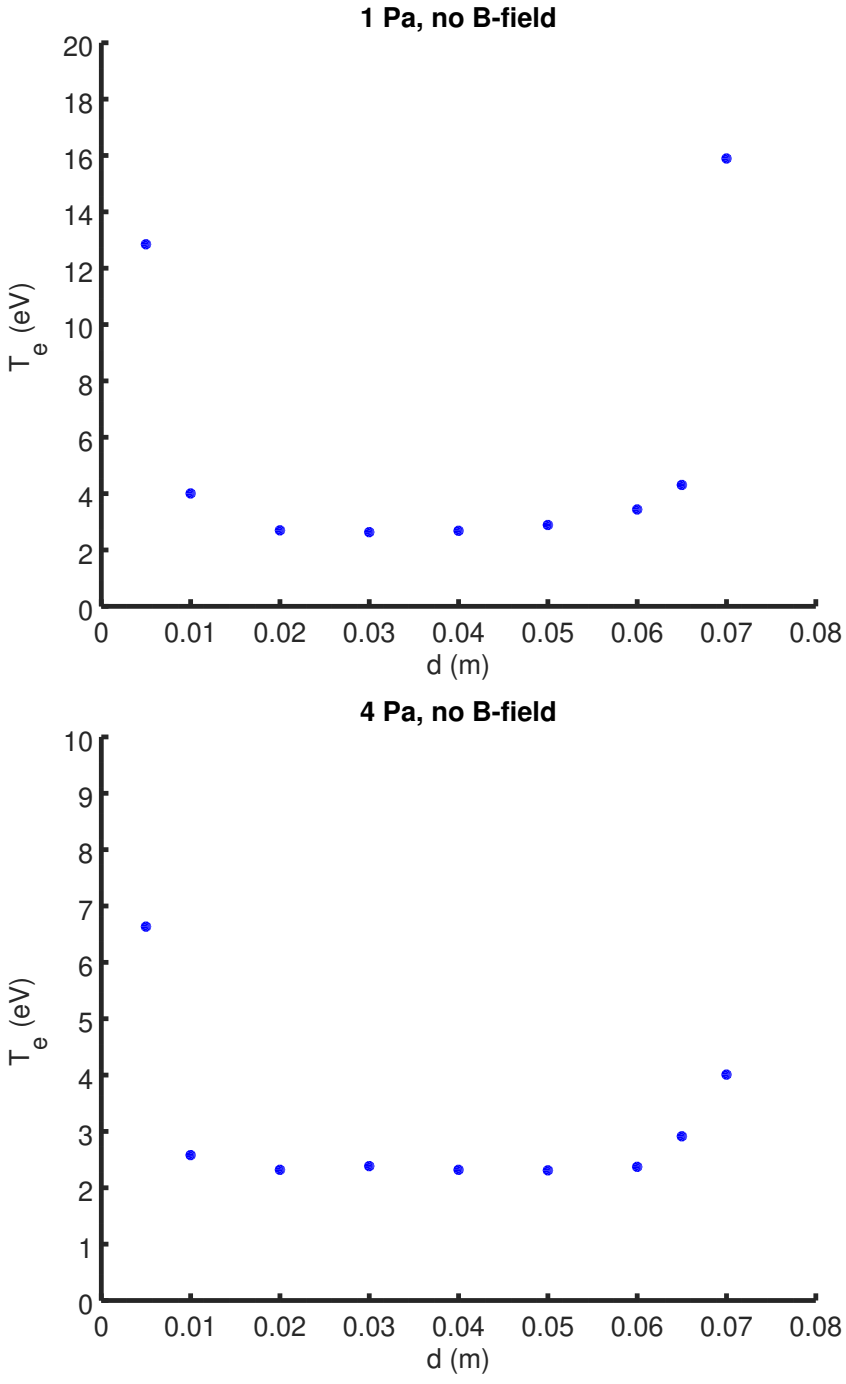

Figure 6.3: Experimental measurements of T_e with no applied magnetic field for 1 Pa (top) and 4 Pa (bottom). Measurements were taken by an emissive probe over 6.5 cm.

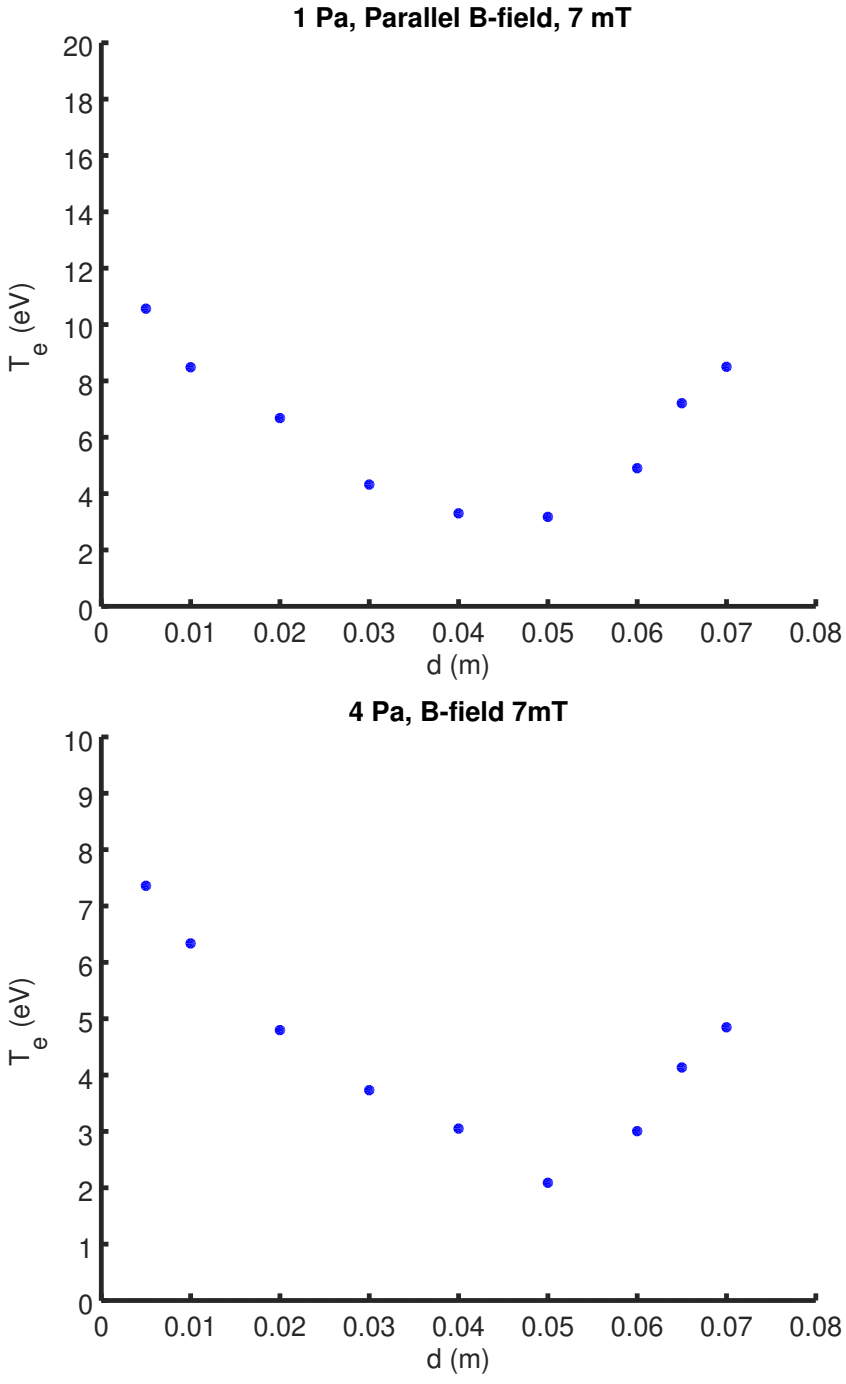

Figure 6.4: Experimental measurements of T_e with an applied parallel magnetic field of 7 mT, for 1 Pa (top) and 4 Pa (bottom), taken with an emissive probe.

6.2 Comparison of 1D Simulation Results with Experimental Data

All simulation results presented in this section are based on our 1D electrostatic PIC code, MagPIC, described in Chapter 2. In comparison with the experiment conducted by the group in IPR, MagPIC represents a drastic simplification since it cannot account for any multi-dimensional effects. Simulation parameters are given in Table 6.1.

Simulation Parameters		
	Un-magnetized	Magnetized
Driving Voltage (V)	100	100
Electrode gap (m)	0.08	0.08
Driving frequency (MHz)	13.56	13.56
Pressure (Pa)	1/4	1/4
B-field strength (T)	-	0.07

Table 6.1: Simulation parameters used in 1D MagPIC for comparison with experiment for un-magnetized and magnetized cases.

6.2.0.1 No Magnetic Field

For the unmagnetized case, at both 1 Pa and 4 Pa, the simulation and experimental data show similar trends of an almost constant electron temperature throughout the bulk plasma and an increase towards the plates near the sheath region. As previously mentioned, this is to be expected due to stochastic heating due to the sheath, which is the dominant heating mechanism at low pressures. Although, experimentally a higher T_e is measured near the plates compared with simulation data.

6.2.0.2 Parallel Magnetic Field

When the parallel magnetic field is applied, an overall increase in bulk T_e is observed, compared to the un-magnetized case. However, as can be seen from Figure 6.6, there is a significant difference in the T_e profiles given by the simulation and experimental data for the magnetized case. In the simulations the trend seems to be consistent with the un-magnetized case showing a constant bulk T_e where as in the experimental case a linear gradient appears to form, creating an increase in T_e from the center of the discharge towards the plates. This feature is not seen in the simulation results, which may indicate the limitations of a 1D comparison.

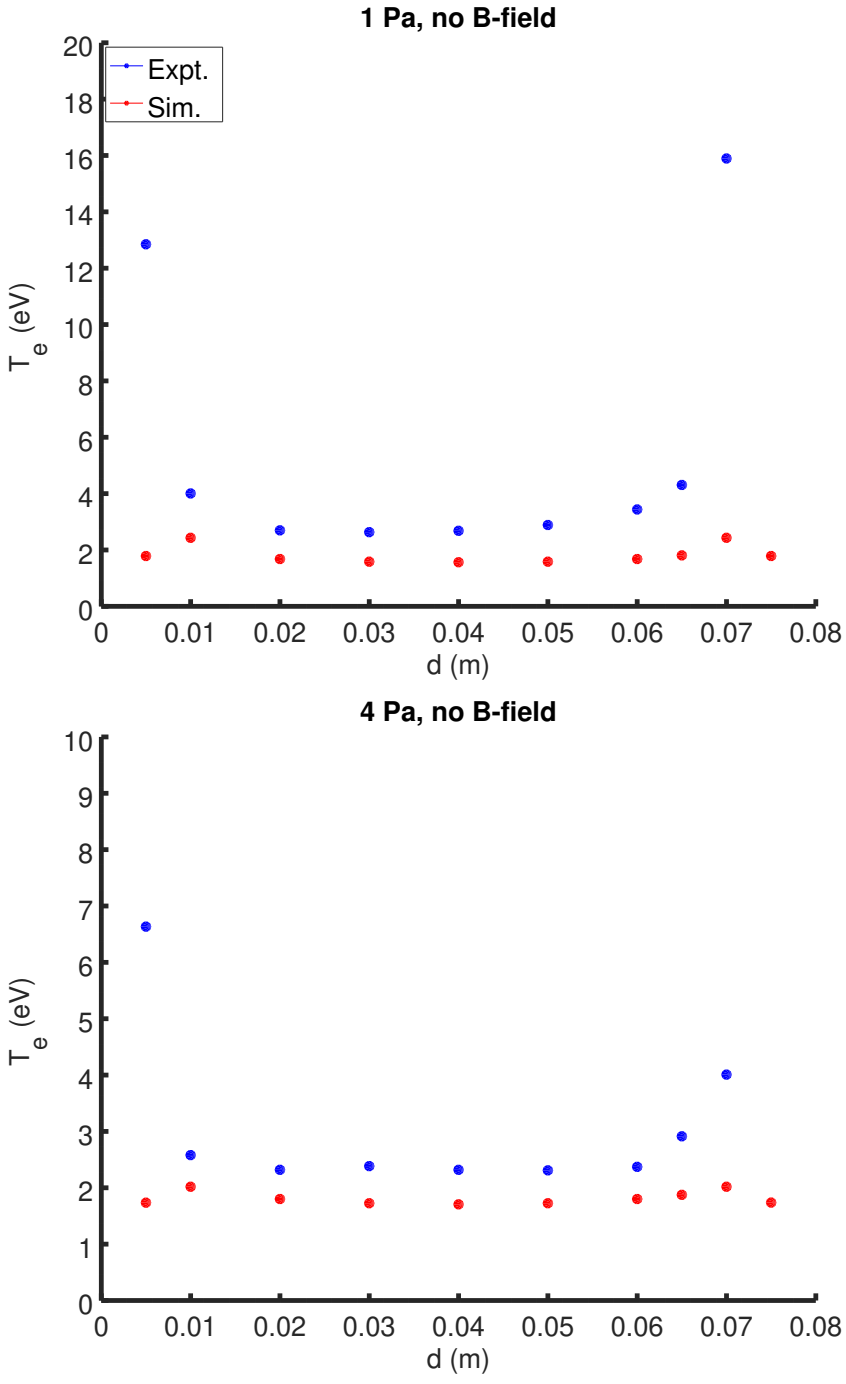

Figure 6.5: Comparison of T_e from experimental measurements and simulation data for un-magnetized case, for 1 Pa (top) and 4 Pa (bottom). Red points represent experimental data while blue points represent simulation data.

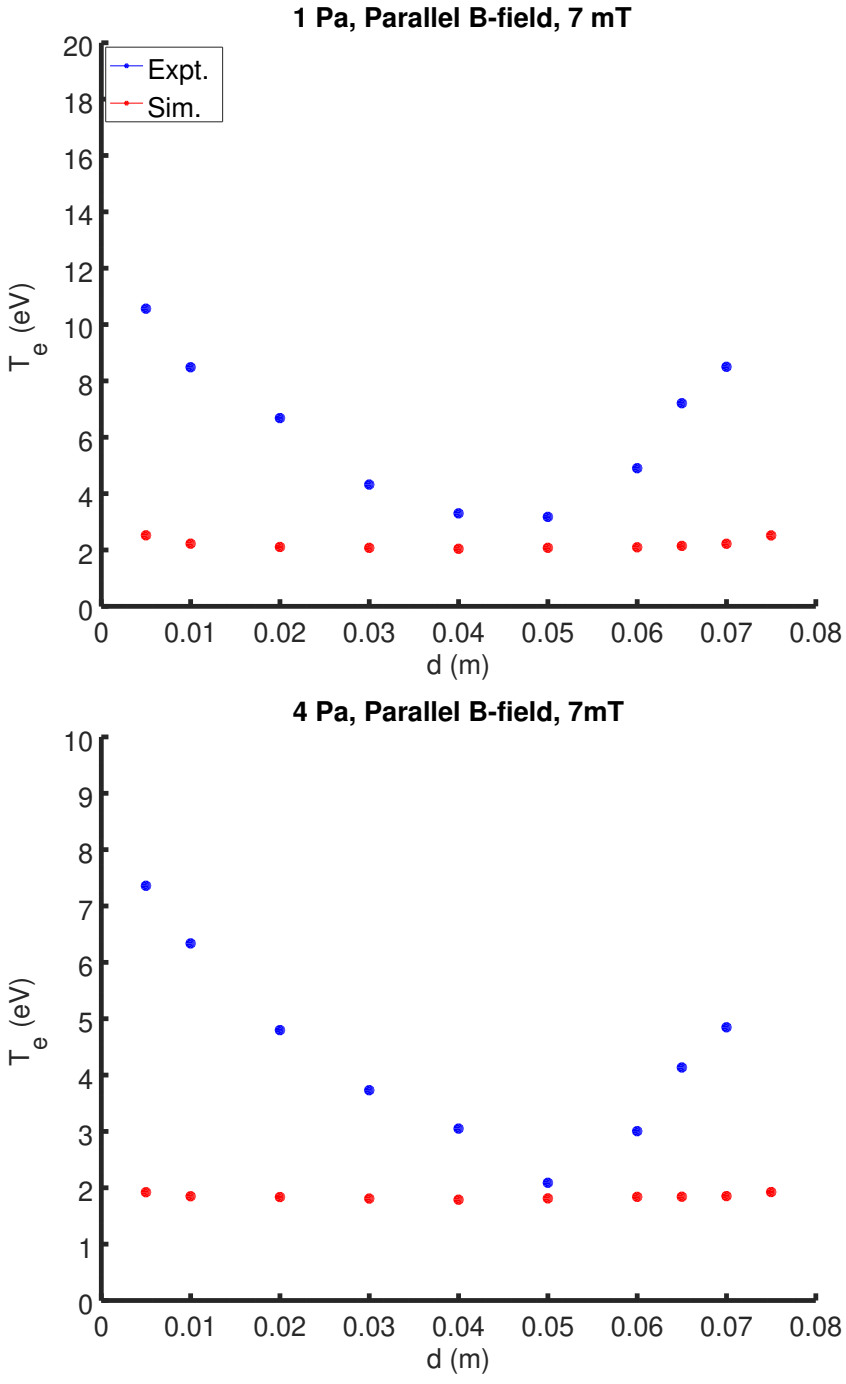

Figure 6.6: Comparison of T_e from experimental measurements and simulation data with a parallel magnetic field of 7 mT, for 1 Pa (top) and 4 Pa (bottom). Red points represent experimental values while blue points represent simulation data.

6.3 2D MagPIC

MagPIC was extended into 2D and some preliminary simulations were performed. The outcome of which have suggested that a comparison of 1D MagPIC simulations with experimental results is not likely to be useful since multi-dimensional effects in the experiment are too pronounced.

In 2D MagPIC, the spatial variation in both the x and y direction is now considered. The simulations are set up with grounded end plates, and push-pull voltages on the other faces. The basic simulation parameters are shown in Table 6.2.

Simulation Parameters 2D MagPIC		
	Case 1	Case 2
Driving Voltage (V)	400	120
Electrode gap (cm)	8	8
Wall to wall gap (cm)	4	4
Driving f (MHz)	13.56	13.56
Gas Density (m^3)	5×10^{21}	5×10^{21}
B-field strength (mT)	5	5
B-field angle (°)	24	24

Table 6.2: Simulation parameters for preliminary 2D MagPIC simulations.

While these preliminary simulations do not closely align with the IPR experimental conditions, they do indicate that good agreement between the 1D MagPIC simulation results and experimental data should not be expected. A particular observation in the 2D simulations is that of strong heating towards the edges of the plasma, as can be seen in Figure 6.7. Consequently,

this suggests that a 1D simulation would not be able to correctly predict the heating relative to the experimental observations.

Upon performing further 1D simulations with nominally the same conditions as the preliminary 2D simulations, we compared the mid-plane densities. Figure 6.8 shows the evolution of the plasma density over 1 RF cycle from the 2D simulations. Here the mid-plane density is typically around $1 \times 10^{15} m^{-3}$ while the bulk density shows shifting in the y-direction over an RF cycle. Figure 6.9 shows the average plasma density over 1 RF cycle from 1D simulations. In this case, the mid-plane density is around $5.5 \times 10^{13} m^{-3}$, significantly less that the 2D value. The discrepancies between the 1D and 2D simulations results further raises concern with the validity of comparing 1D simulations with experimental data. In 1D simulations there are no boundaries in the y or z directions so no side losses of the plasma are accounted for, which means the simulation can over-estimate the plasma density in comparison with experimental results. Comparing the electron fluxes produced by the 1D, Figure 6.11 and 2D simulations, Figure 6.10 further shows more complicated behaviour in the 2D case, mostly like due to the effect of the end plates. That being said, 1D models are still valuable in understanding different phenomena but for this work multi-dimensional effects are too pronounced.

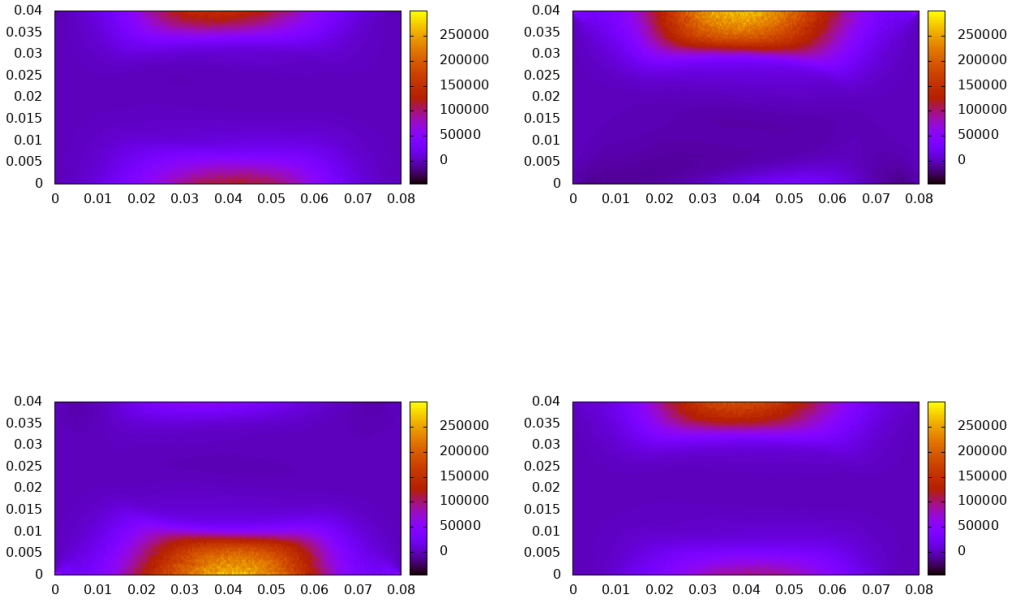

Figure 6.7: Evolution of heating of the edge plasma at various stages over 1 RF cycle for Case 1 described in Table 6.2. Evolution occurs from top left in clockwise direction.

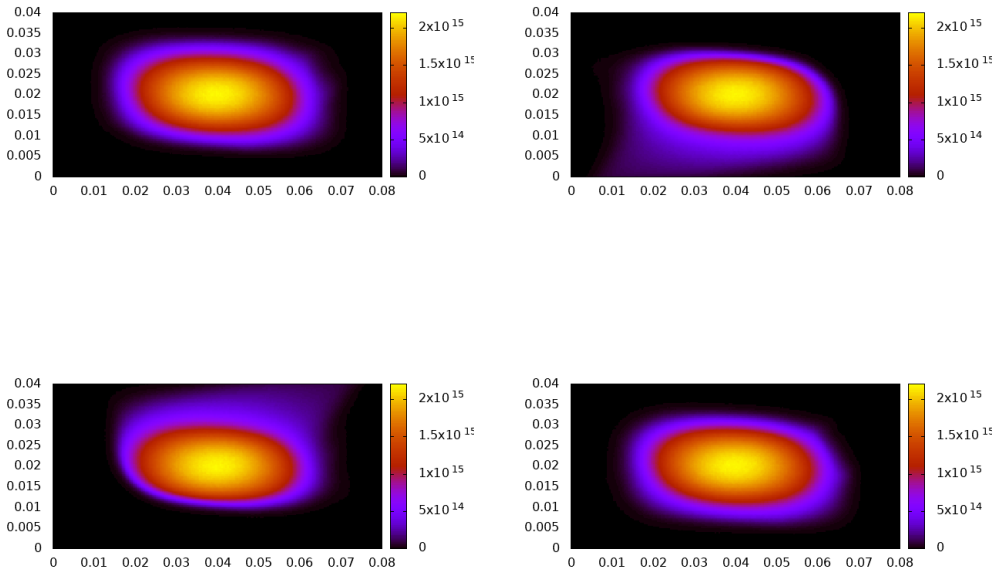

Figure 6.8: Evolution of the plasma density (m^{-3}) at various stages over 1 RF cycle for Case 1 described in Table 6.2 from 2D simulations. Evolution occurs from top left in clockwise direction.

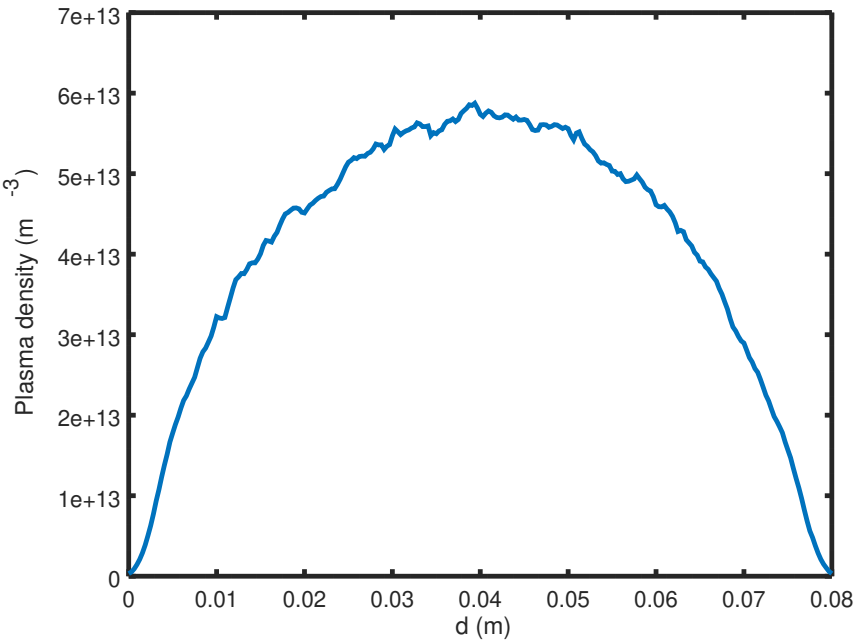

Figure 6.9: Average plasma density over 1 RF cycle from 1D simulations with nominally the same parameters as 2D case.

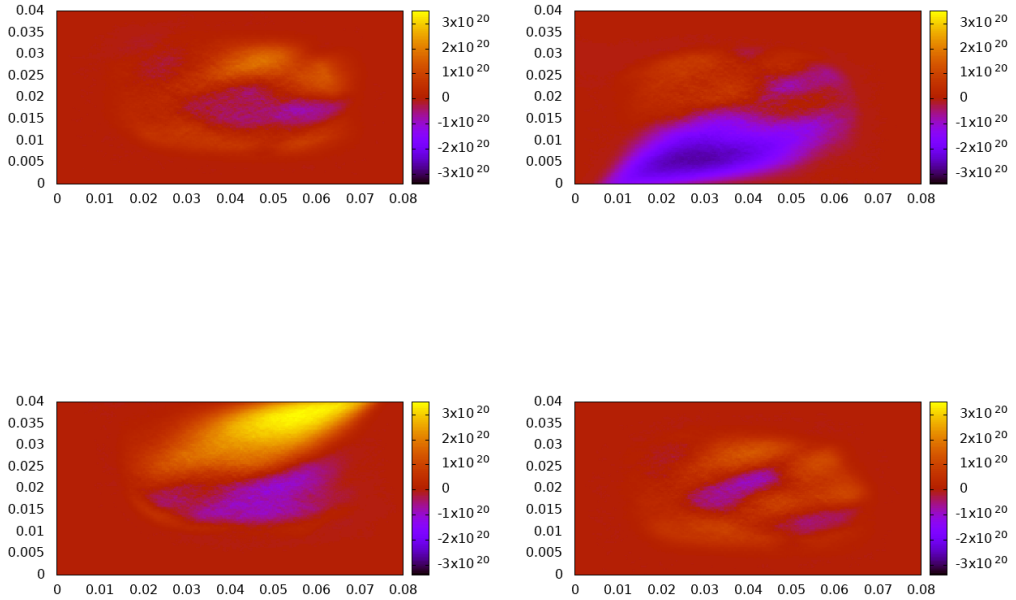

Figure 6.10: Evolution of heating of the electron flux at various stages over 1 RF cycle for Case 1 described in Table 6.2. Evolution occurs from top left in clockwise direction.

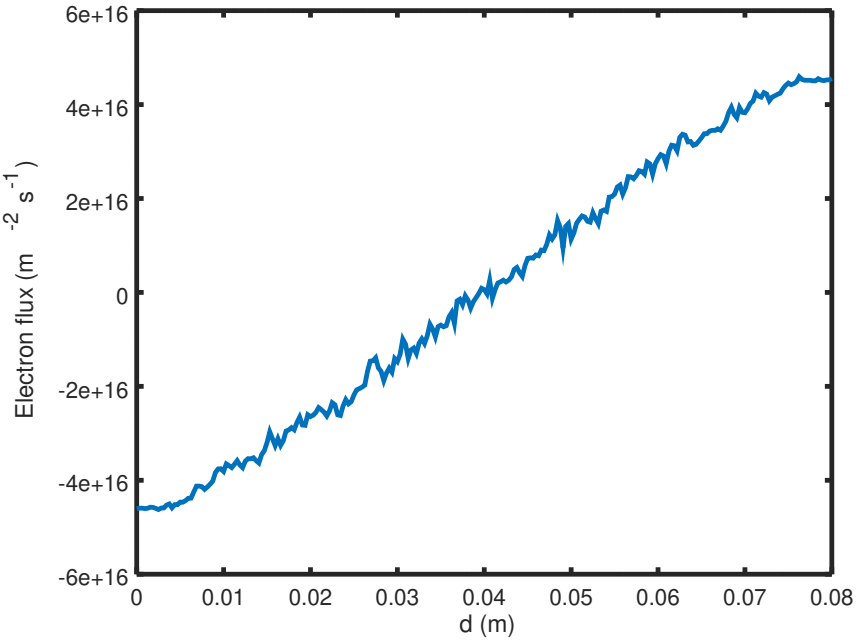

Figure 6.11: Electron flux over 1 RF cycle from 1D simulations with nominally the same parameters as 2D case.

6.4 Discussion and Conclusions

The simulation results offer reasonable agreement with the experimental results for the non-magnetized case. The experimental values are roughly a factor of 2 higher than the simulation values. This proves the marginal validity of MagPIC, for the un-magnetized situation. When the parallel magnetic field is applied, an increase in bulk T_e is observed in both experiment and simulations, compared to the un-magnetized case. In the simulations the trend seems to be consistent with the un-magnetized case showing a constant bulk T_e where as in the experimental case a linear gradient appears to form creating an increase in T_e from the center of the discharge towards the plates. One possible explanation for this inconsistency between the experimental and simulation data for the magnetized case, is due to the $E \times B$ drifts as the 1D simulation can not completely take this effect into account. With a 1d3v PIC model, only the plasma in the domain parallel to the magnetic field is represented. Application of the magnetic field results in a non-uniformly distributed plasma so at least a 2d3v model is needed to describe the magnetized case. This is further suggested from preliminary simulations performed by 2D MagPIC whereby we examine the bulk densities, heating and fluxes and compare with 1D simulation results with nominally the same conditions. This examination highlights that a 1D comparison with experimental results should not provide good agreement since multi-dimensional effects cannot be captured by the 1D simulation.

CHAPTER 7

Conclusions

The objective of this research work is to contribute to the understanding of RF sheaths in the presence of oblique magnetic fields. We have investigated the behaviour of magnetized RF sheaths in a single frequency capacitive discharge primarily with a 1d3v PIC code, MagPIC developed at DCU.

The heart of this thesis is concerned with an effect induced by the application of an oblique magnetic field, namely the magnetized series resonance phenomenon, in a single frequency CCP discharge (Chapter 3). In conventional, single-frequency CCPs the ion fux and energy are coupled and cannot be independently controlled. The ion energy at the surface determines the type of interaction between the plasma and surface, while the ion flux controls the rate of the process therefore independent control of these parameters is desired in plasma processing applications. Following a discussion of some already known methods in over-coming this limitation with single frequency

CCPs, we propose an alternative method through the use of the magnetized series resonance effect whereby the ion energy and flux can become decoupled. An advantage of our proposed method includes the fact that it requires only a single frequency, and that frequency can be low so that electromagnetic effects are not an issue. This motivated the construction a simple model of a magnetized RF-CCP discharge based on coupling a global model and a cold electrical model driven by our simulation results.

We also emphasized the importance of modeling within plasma physics research, particularly PIC modeling when considering the sheath behaviour. There are numerous models of RF sheaths and we briefly touched on some. We then investigated how far conventional simple RF sheath models that do not consider a magnetic field, can be applied in the magnetized situation (Chapter 4). It was found that to a certain extent they can describe the magnetized situation adequately but they have their limits. For this particular study, it appears that RF sheaths can be adequately described by simple models in the presence of an oblique magnetic field, but less so for grazing magnetic field angles, i.e., $\theta > 80°$, which corresponds to angles less than $10°$ with a surface, or exotic circumstances such as the presence of magnetized resonance. We arrived at this conclusion following an comparison of sheath voltages, currents and sheath widths predicted by the model and those calculated by our simulation results. This suggests that the use of such simple models in fusion research, as sheath boundary conditions for models that consider the entire device may prove beneficial.

Part of this thesis involved an elementary comparison between an experimental RF-CCP discharge constructed by the group in IPR, India, and simulation results provided by our 1D MagPIC code (Chapter 5). We examined the measurements of electron temperature obtained experimentally

via an emissive probe with the predictions of the simulation results for both the un-magnetized case and magnetized case, at two different pressures. The agreement between the simulations and experimentally measured data is reasonable, for the un-magnetized cases. While there were obvious discrepancies comparing the magnetized cases. These discrepancies have been attributed to the E×B drift, which is not accounted for in 1D simulation, thereby suggesting that a 1D comparison with experimental results will not prove useful. This idea was further reinforced by preliminary 2D simulations, although simulations did not closely align with the IPR experimental conditions, they still indicated that good agreement between the 1D MagPIC simulation results and experimental data should not be expected.

Future work could include further investigation in to the use of the magnetized series resonance effect in obtaining independent control of ion flux and energy - i.e., determining the optimal discharge conditions. While also simulating this effect with 2D MagPIC.

Bibliography

[1] Gregory Dominique Dubus. From plain visualisation to vibration sensing: using a camera to control the flexibilities in the ITER remote handling equipment. Tampere University of Technology, 2014.

[2] DD Tskhakaya Sr and L Kos. Stability of the magnetized plasma-wall transition layer. *Physics of Plasmas*, 22(9):092117, 2015.

[3] Charles K Birdsall. Particle-in-cell charged-particle simulations, plus monte carlo collisions with neutral atoms, pic-mcc. *IEEE Transactions on plasma science*, 19(2):65–85, 1991.

[4] Brian G Heil, Uwe Czarnetzki, Ralf Peter Brinkmann, and Thomas Mussenbrock. On the possibility of making a geometrically symmetric rf-ccp discharge electrically asymmetric. *Journal of Physics D: Applied Physics*, 41(16):165202, 2008.

[5] J Schulze, E Schüngel, and U Czarnetzki. The electrical asymmetry effect in capacitively coupled radio frequency discharges–measurements

of dc self bias, ion energy and ion flux. *Journal of Physics D: Applied Physics*, 42(9):092005, 2009.

[6] S Binwal, JK Joshi, SK Karkari, PK Kaw, and L Nair. Passive inference of collision frequency in magnetized capacitive argon discharge. *Physics of Plasmas*, 25(3):033506, 2018.

[7] A Kirk. Nuclear fusion: bringing a star down to earth. *Contemporary Physics*, 57(1):1–18, 2016.

[8] Quamrul Haider. Nuclear fusion: Holy grail of energy. In *Nuclear Fusion-One Noble Goal and a Variety of Scientific and Technological Challenges*. IntechOpen, 2019.

[9] ITER Organisation. Iter:the way to new energy, 2019. `https://www.iter.org/`, Last accessed on 2019-11-07.

[10] V Bergeaud, L-G Eriksson, and DFH Start. Iter relevant icrf heating scenarios with large ion heating fraction. *Nuclear fusion*, 40(1):35, 2000.

[11] Dani Gallart, Mervi Mantsinen, and Yevgen Kazakov. Heating bulk ions in demo with icrf waves. In *BSC Doctoral Symposium (2nd: 2015: Barcelona)*, pages 106–107. Barcelona Supercomputing Center, 2015.

[12] FW Perkins. Radiofrequency sheaths and impurity generation by icrf antennas. *Nuclear Fusion*, 29(4):583, 1989.

[13] JR Myra, DA D'Ippolito, and MJ Gerver. Faraday screen sheaths and impurity production during ion cyclotron heating. *Nuclear fusion*, 30(5):845, 1990.

[14] G Van Oost, R Van Nieuwenhove, R Koch, AM Messiaen, PE Vandenplas, RR Weynants, KH Dippel, KH Finken, YT Lie, A Pospieszczyk, et al. Icrf/edge physics research on textor. *Fusion Engineering and Design*, 12(1-2):149–170, 1990.

[15] CC Klepper, A Lasa, D Borodin, A Kirschner, M Groth, P Jacquet, V Bobkov, L Colas, and JET Contributors Team. Evaluating localized surface erosion from rf-sheath interactions in jet with an ITER-like wall. *APS*, 2015:TP12–167, 2015.

[16] Irving Langmuir. Oscillations in ionized gases. *Proceedings of the National Academy of Sciences of the United States of America*, 14(8):627, 1928.

[17] José A Bittencourt. *Fundamentals of plasma physics*. Springer Science & Business Media, 2013.

[18] BR Adhikari and R Khanal. Introduction to the plasma state of matter. *Himalayan Physics*, 4:60–64, 2013.

[19] Alexander Fridman and Lawrence A Kennedy. *Plasma physics and engineering*. CRC press, 2004.

[20] Michael G Kong, G Kroesen, G Morfill, T Nosenko, Toshimi Shimizu, J Van Dijk, and JL Zimmermann. Plasma medicine: an introductory review. *new Journal of Physics*, 11(11):115012, 2009.

[21] Cornelis Marius Braams and Peter E Stott. *Nuclear fusion: half a century of magnetic confinement fusion research*. CRC Press, 2002.

[22] Alexander Piel. *Plasma Physics An Introduction to Laboratory, Space, and Fusion Plasmas*. Springer-Verlag Berlin Heidelberg 2010, 2010.

[23] Francis F Chen. *Introduction to plasma physics*. Springer Science & Business Media, 2012.

[24] Paul M Bellan. *Fundamentals of plasma physics*. Cambridge University Press, 2008.

[25] KH You, SJ You, DW Kim, BK Na, BH Seo, JH Kim, and HY Chang. Measurement and analysis of electron-neutral collision frequency in the calibrated cutoff probe. *Physics of Plasmas*, 23(3):033509, 2016.

[26] K-U Riemann. The bohm criterion and sheath formation. *Journal of Physics D: Applied Physics*, 24(4):493, 1991.

[27] Noah Hershkowitz. Sheaths: More complicated than you think. *Physics of Plasmas*, 12(5):055502, 2005.

[28] S Devaux, E Faudot, J Moritz, and S Heuraux. Aline: A device dedicated to understanding radio-frequency sheaths. *Nuclear Materials and Energy*, 12:908–912, 2017.

[29] RN Franklin. Where is the sheath edge? *Journal of Physics D: Applied Physics*, 37(9):1342, 2004.

[30] Peter C Stangeby. *The plasma boundary of magnetic fusion devices*. CRC Press, 2000.

[31] AV Gurevich and NT Pashchenko. Space charge sheath formation in a magnetized plasma flow around space bodies. *Acta Astronautica*, 10(2):91–97, 1983.

[32] David Bohm. The characteristics of electrical discharges in magnetic fields. *Qualitative Description of the Arc Plasma in a Magnetic Field*, 1949.

[33] Pascal Chabert and Nicholas Braithwaite. *Physics of radio-frequency plasmas*. Cambridge University Press, 2011.

[34] Spilios Riyopoulos. Effects of static magnetic fields on rf-driven plasma sheaths. *Physics of Plasmas*, 3(7):2511–2522, 1996.

[35] C Plechaty, R Presura, S Wright, S Neff, and A Haboub. Penetration of plasma across a magnetic field. *Astrophysics and Space Science*, 322(1-4):195–199, 2009.

[36] R Chodura. Plasma–wall transition in an oblique magnetic field. *Physics of Fluids (1958-1988)*, 25(9):1628–1633, 1982.

[37] J Van Dijk, GMW Kroesen, and A Bogaerts. Plasma modelling and numerical simulation. *Journal of Physics D: Applied Physics*, 42(19):190301, 2009.

[38] HC Kim, Felipe Iza, SS Yang, M Radmilović-Radjenović, and JK Lee. Particle and fluid simulations of low-temperature plasma discharges: benchmarks and kinetic effects. *Journal of Physics D: Applied Physics*, 38(19):R283, 2005.

[39] Charles K Birdsall and A Bruce Langdon. *Plasma physics via computer simulation*. CRC Press, 2004.

[40] Roger W Hockney and James W Eastwood. *Computer simulation using particles*. CRC Press, 1988.

[41] Miles M Turner. Kinetic properties of particle-in-cell simulations compromised by monte carlo collisions. *Physics of Plasmas (1994-present)*, 13(3):033506, 2006.

[42] TG Jenkins and DN Smithe. Benchmarking sheath subgrid boundary conditions for macroscopic-scale simulations. *Plasma Sources Science and Technology*, 24(1):015020, 2014.

[43] D Krauss-Varban. From theoretical foundation to invaluable research tool: Modern hybrid simulations. *arXiv preprint physics/0610133*, 2006.

[44] Andrew Hurlbatt, Andrew Robert Gibson, Sandra Schröter, Jérôme Bredin, Alexander Paul Stuart Foote, Pascaline Grondein, Deborah O'Connell, and Timo Gans. Concepts, capabilities, and limitations of global models: a review. *Plasma Processes and Polymers*, 14(1-2):1600138, 2017.

[45] Michael A Lieberman and Alan J Lichtenberg. *Principles of plasma discharges and materials processing*. John Wiley & Sons, 2005.

[46] Tomonori Takizuka. Modeling and simulation on sol-divertor plasmas. In *AIP Conference Proceedings*, volume 1237, pages 138–152. AIP, 2010.

[47] Ivona Vasileska, Leon Kos, David Tskhakaya, Richard Pitts, and Tomaz Gyergyek. Pic kinetic modelling for elm transport in the scrape-off layer. In *26th Int. Conf. Nuclear Energy for New Europe, pages*, pages 708–1.

[48] Z Donkó, J Schulze, BG Heil, and U Czarnetzki. Pic simulations of the separate control of ion flux and energy in ccrf discharges via the electrical asymmetry effect. *Journal of Physics D: Applied Physics*, 42(2):025205, 2008.

[49] Trenton J Godar. Testing of two novel semi-implicit particle-in-cell techniques. 2014.

[50] D Tskhakaya, K Matyash, R Schneider, and F Taccogna. The particle-in-cell method. *Contributions to Plasma Physics*, 47(8-9):563–594, 2007.

[51] Cross sections extracted from program magboltz, version 7.1 june 2004, stephen francis biagi. `http://www.lxcat.laplace.univ-tlse.fr`.

[52] RN Franklin. The plasma–sheath boundary region. *Journal of Physics D: Applied Physics*, 36(22):R309, 2003.

[53] JE Allen. The plasma–sheath boundary: its history and langmuir's definition of the sheath edge. *Plasma Sources Science and Technology*, 18(1):014004, 2008.

[54] Yicheng Wang. Practical definition of the plasma sheath edge for modeling planar glow discharges. *Applied Physics Letters*, 66(18):2329–2330, 1995.

[55] Valery Godyak and Natalia Sternberg. On the consistency of the collisionless sheath model. *Physics of Plasmas*, 9(11):4427–4430, 2002.

[56] Joaquim Loizu, Paolo Ricci, and Christian Theiler. Existence of subsonic plasma sheaths. *Physical Review E*, 83(1):016406, 2011.

[57] Natalia Sternberg and Valery Godyak. The bohm plasma-sheath model and the bohm criterion revisited. *IEEE Transactions on Plasma Science*, 35(5):1341–1349, 2007.

[58] E Schüngel, D Eremin, J Schulze, T Mussenbrock, and U Czarnetzki. The electrical asymmetry effect in geometrically asymmetric capacitive

radio frequency plasmas. *Journal of Applied Physics*, 112(5):053302, 2012.

[59] E Kawamura, V Vahedi, MA Lieberman, and CK Birdsall. Ion energy distributions in rf sheaths; review, analysis and simulation. *Plasma Sources Science and Technology*, 8(3):R45, 1999.

[60] PC Boyle, AR Ellingboe, and MM Turner. Independent control of ion current and ion impact energy onto electrodes in dual frequency plasma devices. *Journal of Physics D: Applied Physics*, 37(5):697, 2004.

[61] Hans-Dirk Löwe, Haruhiro H Goto, and Tadahiro Ohmi. Control of ion energy and flux in a dual radio frequency excitation magnetron sputtering discharge. *Journal of Vacuum Science & Technology A: Vacuum, Surfaces, and Films*, 9(6):3090–3099, 1991.

[62] Zoltán Donkó and Zoran Lj Petrović. Ion behavior in capacitively-coupled dual-frequency discharges. In *Journal of Physics: Conference Series*, volume 86, page 012011. IOP Publishing, 2007.

[63] PC Boyle, AR Ellingboe, and MM Turner. Electrostatic modelling of dual frequency rf plasma discharges. *Plasma Sources Science and Technology*, 13(3):493, 2004.

[64] T Gans, J Schulze, D Oconnell, U Czarnetzki, R Faulkner, AR Ellingboe, and MM Turner. Frequency coupling in dual frequency capacitively coupled radio-frequency plasmas. *Applied Physics Letters*, 89(26):261502, 2006.

[65] U Czarnetzki, BG Heil, J Schulze, Z Donkó, T Mussenbrock, and RP Brinkmann. The electrical asymmetry effect-a novel and simple

method for separate control of ion energy and flux in capacitively coupled rf discharges. In *Journal of Physics: Conference Series*, volume 162, page 012010. IOP Publishing, 2009.

[66] Ihor Korolov, Zoltán Donkó, Uwe Czarnetzki, and Julian Schulze. The effect of the driving frequencies on the electrical asymmetry of dual-frequency capacitively coupled plasmas. *Journal of Physics D: Applied Physics*, 45(46):465205, 2012.

[67] T Lafleur, PA Delattre, EV Johnson, and JP Booth. Separate control of the ion flux and ion energy in capacitively coupled radio-frequency discharges using voltage waveform tailoring. *Applied Physics Letters*, 101(12):124104, 2012.

[68] Julian Schulze, E Schüngel, Z Donkó, and Uwe Czarnetzki. The electrical asymmetry effect in multi-frequency capacitively coupled radio frequency discharges. *Plasma Sources Science and Technology*, 20(1):015017, 2011.

[69] Aranka Derzsi, Ihor Korolov, Edmund Schüngel, Zoltán Donkó, and Julian Schulze. Electron heating and control of ion properties in capacitive discharges driven by customized voltage waveforms. *Plasma Sources Science and Technology*, 22(6):065009, 2013.

[70] T Lafleur. Tailored-waveform excitation of capacitively coupled plasmas and the electrical asymmetry effect. *Plasma Sources Science and Technology*, 25(1):013001, 2015.

[71] Jan Trieschmann, Mohammed Shihab, Daniel Szeremley, Abd Elfattah Elgendy, Sara Gallian, Denis Eremin, Ralf Peter Brinkmann, and Thomas Mussenbrock. Ion energy distribution functions behind the

sheaths of magnetized and non-magnetized radio frequency discharges. *Journal of Physics D: Applied Physics*, 46(8):084016, 2013.

[72] Shali Yang, Ya Zhang, Hongyu Wang, Jianwei Cui, and Wei Jiang. Magnetical asymmetric effect in geometrically and electrically symmetric capacitively coupled plasma. *Plasma Processes and Polymers*, 14(12):1700087, 2017.

[73] Shali Yang, Lijie Chang, Ya Zhang, and Wei Jiang. Magnetical asymmetry effect in capacitively coupled plasmas: effects of the magnetic field gradient, pressure, and gap length. *Plasma Sources Science and Technology*, 27(3):035008, 2018.

[74] M Oberberg, J Kallähn, P Awakowicz, and J Schulze. Experimental investigations of the magnetic asymmetry effect in capacitively coupled radio frequency plasmas. *Plasma Sources Science and Technology*, 27(10):105018, 2018.

[75] Weiguag Qiu. *Electron series resonance plasma discharges: Unmagnetized and magnetized*. PhD thesis, Electrical Engineering and Computer Science, 2001.

[76] Hyo-Chang Lee and Chin-Wook Chung. Impedance transition and series resonance between bulk plasma and sheath in biased inductively coupled plasma. *Thin Solid Films*, 518(18):5219–5222, 2010.

[77] DJ Cooperberg and CK Birdsall. Series resonance sustained plasmas in a metal bound plasma slab. *Plasma Sources Science and Technology*, 7(2):96, 1998.

[78] BM Annaratone, VPT Ku, and JE Allen. Identification of plasma-sheath resonances in a parallel-plate plasma reactor. *Journal of Applied Physics*, 77(10):5455–5457, 1995.

[79] Biswajit Bora, H Bhuyan, M Favre, E Wyndham, H Chuaqui, and M Kakati. Measurements of time average series resonance effect in capacitively coupled radio frequency discharge plasma. *Physics of Plasmas*, 18(10):103509, 2011.

[80] Biswajit Bora, H Bhuyan, M Favre, E Wyndham, and H Chuaqui. Theoretical approach for plasma series resonance effect in geometrically symmetric dual radio frequency plasma. *Applied Physics Letters*, 100(9):094103, 2012.

[81] Z Donkó, J Schulze, U Czarnetzki, and D Luggenhölscher. Self-excited nonlinear plasma series resonance oscillations in geometrically symmetric capacitively coupled radio frequency discharges. *Applied Physics Letters*, 94(13):131501, 2009.

[82] JK Joshi, S Binwal, SK Karkari, and Sunil Kumar. Electron series resonance in a magnetized 13.56 mhz symmetric capacitive coupled discharge. *Journal of Applied Physics*, 123(11):113301, 2018.

[83] J Taillet. Resonance-sustained radio frequency discharges. *American Journal of Physics*, 37(4):423–441, 1969.

[84] Thomas Mussenbrock and Ralf Peter Brinkmann. Nonlinear electron resonance heating in capacitive radio frequency discharges. *Applied physics letters*, 88(15):151503, 2006.

[85] Edmund Schüngel, S Brandt, Zoltán Donkó, I Korolov, A Derzsi, and

Julian Schulze. Electron heating via self-excited plasma series resonance in geometrically symmetric multi-frequency capacitive plasmas. *Plasma Sources Science and Technology*, 24(4):044009, 2015.

[86] Victor PT Ku, Beatrice M Annaratone, and John E Allen. Plasma-sheath resonances and energy absorption phenomena in capacitively coupled radio frequency plasmas. part i. *Journal of Applied Physics*, 84(12):6536, 1998.

[87] Valery A Godyak. *Soviet radio frequency discharge research*. Delphic Associates, 1986.

[88] R Lucken, A Bourdon, MA Lieberman, and P Chabert. Instability-enhanced transport in low temperature magnetized plasma. *Physics of Plasmas*, 26(7):070702, 2019.

[89] Naohiko Goto. Energy control of ions from a capacitively coupled plasma using rf resonance method. *Japanese journal of applied physics*, 38(7S):4357, 1999.

[90] Naohiko Goto. Dependence of resonance condition on pressure in an rf resonance method. *IEEE transactions on plasma science*, 27(5):1353–1357, 1999.

[91] Natalia Sternberg, Valery Godyak, and Daniel Hoffman. Magnetic field effects on gas discharge plasmas. *Physics of Plasmas*, 13(6):063511, 2006.

[92] Zhong-ling Dai and You-nian Wang. Characteristics of single and dual radio-frequency (rf) plasma sheaths. *Frontiers of Physics in China*, 1(2):178–185, 2006.

[93] VA Godyak, RB Peijak, and N Sternberg. A comparison of rf electrode sheath models. *IEEE transactions on plasma science*, 21(4):378–382, 1993.

[94] CD Child. Discharge from hot cao. *Physical Review (Series I)*, 32(5):492, 1911.

[95] Irving Langmuir. The interaction of electron and positive ion space charges in cathode sheaths. *Physical Review*, 33(6):954, 1929.

[96] Samuel J Langendorf. *Effects of electron emission on plasma sheaths*. PhD thesis, Georgia Institute of Technology, 2015.

[97] Michael A Lieberman. Analytical solution for capacitive rf sheath. *Plasma Science, IEEE Transactions on*, 16(6):638–644, 1988.

[98] Miles M Turner and Pascal Chabert. A radio-frequency sheath model for complex waveforms. *Applied Physics Letters*, 104(16):164102, 2014.

[99] Martin Greenwald. Beyond benchmarkinghow experiments and simulations can work together in plasma physics. *Computer physics communications*, 164(1-3):1–8, 2004.

[100] Shikar Binwall. personal communication, 24-05-2016.

[101] JP Sheehan and N Hershkowitz. Emissive probes. *Plasma Sources Science and Technology*, 20(6):063001, 2011.